Variety of the drift pumice clasts from the 2021 Fukutoku-Oka-no-Ba eruption, Japan.

Kenta Yoshida*, Yoshihiko Tamura, Tomoki Sato, Takeshi Hanyu, Yoichi Usui, Qing Chang, Shigeaki Ono

Research Institute for Marine Geodynamics, Japan Agency for Marine-Earth Science and Technology, Natsushima-cho 2-15, Yokosuka, 237-0061 Japan.

Correspondence
Kenta Yoshida, Natsushima-cho 2-15, Yokosuka, 237-0061 Japan.
E-mail: yoshida_ken@jamstec.go.jp

Funding Information

Japan Society for the Promotion of Science, KAKENHI, Grant Nos. JP19K14825 and JP19H01999 to K.Y. and JP21H01195 to Y. T.
The Joint Usage and Research Program of the Earthquake Research Institute, the University of Tokyo, No. ERI JURP 2021-B-01.
NOZOMI Farm.

Conflict of interest disclosure

There are no entities or relationship, etc. presenting a potential conflict of interest requiring disclosure in relation to this manuscript.

This is an accepted version of the preprint modified after the reviews under the submission to Island Arc. The published article is available from https://doi.org/10.1111/iar.12441 as an open access article.

Abstract

Pumice rafts that arrived at the Nansei Islands, Japan, provided a unique opportunity to investigate the Fukutoku-Oka-no-Ba (FOB) eruption of August 2021. Despite drifting for two months for ~1300 km, the drift pumice raft had a large volume and contained a variety of pumice clasts, some of which were deposited during a high tide in a typhoon, while others were washed up on a sandy beach. Most of the drift pumice clasts are gray in color, vesicular, and have a groundmass containing black enclaves. Rare black pumice and the main gray pumice components have similar trachytic compositions, with SiO_2 = 61–62 mass% and total alkalis = 8.6–10 mass% (on an anhydrous basis). Both pumice types contain clinopyroxene, plagioclase, and rare olivine phenocrysts. Thin-section observations show that the gray pumice has more elongated vesicles as compared with the black pumice that has spherical vesicles, even where the two types of pumice are in the same clast. The glass in the black pumice is transparent and brown in color, while that in the gray pumice is colorless. No micro or nano-crystals were observed during electron and optical microscopy. Raman spectra of the brown-colored glass exhibit a clear magnetite peak, suggesting magnetite nanolites cause the brown color. High-Mg olivine in the black pumice has an equilibrium temperature of c. 1200 °C and a rim diffusion profile indicative of re-equilibration with the surrounding melt over a period of hours to days.

The textural relationships between the gray and black pumice suggest that the black pumice had become black and viscous before the two types of pumice mixed. Therefore, crystallization of magnetite nanolites and a corresponding increase in melt viscosity were important in the eruption preparation process, which then resulted in a large-scale Plinian eruption.

Keywords: Fukutoku-Oka-no-Ba, Izu-Bonin-Mariana arc, Plinian eruption, drift pumice, nanolite

1. Introduction

Fukutoku-Oka-no-Ba (FOB) volcano is located at 24°17.1’N/141°28.9’E, ~5 km north-east to Minami-Ioto Island, south of mainland Japan (Fig. 1a). Five eruptions have been recorded in 1904-05, 1914, 1986, 2005, and 2010 (https://www1.kaiho.mlit.go.jp/GIJUTSUKOKUSAI/kaiikiDB/kaiyo24-2.htm), and discoloration of the sea surface has been occasionally observed (e.g., Furukawa, 1995). Geochemical analyses and petrographical observations have been conducted on pumice erupted in 1904, 1914, and 1986 (Tsuya, 1937; Yoshida et al., 1987; Kato, 1988; Nakano & Kawanabe, 1992). Major element composition the FOB pumices are trachyte similar to the nearby Ioto volcano, which magma type is rare in the Izu-Ogasawara arc. In contrast, FOB pumices are isotopically distinct from the products of the Ioto, but similar to the Hiyoshi Volcanic Complex to the south of the FOB (Sun et al., 1998).

Detailed topography and preliminary geophysical observations of the relevant area show that there exists a large volcanic complex, which has a size of 15 and 30 km for EW and NS direction, respectively, and rises 2000–2200 m above the surrounding ocean floor (Fig. 1b). This complex consists of Kita-Fukutoku-Tai, Kita-Fukutoku caldera, and Minami-Ioto volcanoes, from north to south (Ito et al., 2011). The Kita-Fukutoku caldera has east-west and north-south length of 10 and 16 km, respectively (Fig. 1b). The seismic basement of the caldera has a mortar shape, which is filled by low velocity and low density materials (Onodera et al., 2003). Nishizawa et al. (2002) suggested the existence of partial melts below the caldera at >1.5–2 km beneath the sea level. FOB is a central cone of the Kita-Fukutoku caldera, which has ~2 km in diameter at the bottom and the height is ~200 m. The summit of FOB had an oval shape elongated NE-SW, with the lengths of 1.5 km and 1 km, respectively, and was flat at the depth of ~30 m below sea level before the eruption (Ito et al., 2011).
The 2021 FOB Plinian eruption occurred from 04:30 (JST, Japan Standard Time, UTC + 9:00) on 13 August, reported by a local fisherman, to the morning of 16 August (Japan Meteorological Agency, 2021). The eruption column reached 16 km in height, the tropopause of the relevant area. The total volume of the erupted pumices was estimated to be 100–500 × 10^6 m^3 (Oikawa et al., 2021). These pumices were ejected high in the air, fell on the ocean surface and started floating. A large pumice raft was observed by satellite images at 08:00, 3–4 h after the eruption started (Ikegami, 2021). After the eruption, two small islands were observed as "( )" shape, then the eastern disappeared within a month (Geospatial Information Authority of Japan, 2021).
Pumice rafting is typically observed once a decade worldwide (e.g., Bryan et al., 2012), where silicic magma erupted explosively beneath the ocean. The 1986 FOB eruption also generated pumice rafts, and large amounts of drift pumice clasts arrived at numerous locations, including the Nansei Islands, to where the pumice clasts were transported for ~1300 km by the Kuroshio Counter-current after a duration of >4 months (Fig. 1a; Yoshida et al., 1987; Kato, 1988; Mori et al., 1992). An ocean bottom observatory instrument installed near Nishinoshima accidentally drifted from the Izu–Bonin arc towards the Nansei Islands in 2020, which are ~ 1700 km apart (Tada et al., 2021). Ocean current simulations indicate that the drift from the Izu–Bonin arc to the Nansei Islands takes <6 months, but depends on the seasonal current and wind conditions (Tada et al., 2021).
The 2021 FOB pumice rafts traveled westward after the eruption. The RV *Keifu-Maru* of the Japan Meteorological Agency collected samples of floating pumices at 25°30.3'N/138°53.3'E on 22 August 2021 (Japan Meteorological Agency, 2021). Subsequently, the drift pumice rafts arrived at the Nansei Islands in early October, ~2 months after the eruption. Drifting of pumice continued along the Kuroshio current and arrived at the shores of Kanto area and Izu Islands in Mid-November. From the southwest Japan to eastern area, drifting pumice followed a large-meandering of the Kuroshio Current (e.g., Aoki et al., 2020) and might have drifted along the offshore path (Fig. 1a). The 2021 pumice raft drifted twice as fast as the 1986 FOB pumice raft, possibly due to the seasonal change of the Kuroshio

Counter-current that is thought to be weakened in the winter season (Uchiyama et al., 2016). We undertook comprehensive analyses of the *Keifu-Maru* samples and drift pumice clasts collected from several locations on the Nansei Islands. Petrographic observations revealed a variety of pumice types originated from the 2021 eruption. In the present paper, we describe the textural and geochemical characteristics of the collected pumice clasts, and discuss the mechanisms of the 2021 FOB eruption.

2. Methods

Mineral compositions were determined with a field emission gun electron microprobe (EPM) analyzer equipped with five wavelength-dispersive X-ray detectors (JXA-8500F; JEOL) at Japan Agency for Marine-Earth Science and Technology (JAMSTEC; Yokosuka, Japan). Natural and synthetic standards were used to calibrate the quantitative analyses. The analytical conditions were 15 kV and 10 nA for the accelerating voltage and beam current, respectively, except for the olivine analyses. For olivine, we used an accelerating voltage of 20 kV and beam current of 25 nA. Beam diameter was set to 3 μm for minerals and 5 μm for glass.

Raman spectra were obtained with a Raman spectrophotometer (RAMANtouch VIS-HP-MAST; Nanophoton) equipped with a 532 nm semiconductor green laser at JAMSTEC. The laser power on the sample surface was ~2 mW, and data were acquired in 2 × 20 s cycles. The spectrometer was calibrated to the Raman peak of a Si wafer (520.7 cm^{-1}).

Whole-rock major element compositions of the pumice clasts were determined by X-ray fluorescence (XRF) spectrometry (Rigaku ZSX Primus II) following the analytical procedure of Tani et al. (2006) and sample preparation methods of Sato et al. (2020). Prior to analysis, the pumice samples were crushed to pebble size (5-10 mm) and soaked in hot water (~40 °C) for 0–3 days. The clasts were then repeatedly boiled in Milli-Q water in a microwave oven until addition of a $AgNO_3$ solution showed that precipitation of AgCl did not occur. After desalinization, all samples were washed with Milli-Q water and acetone in an ultrasonic bath, and powdered in an agate mortar or with a Multi-beads Shocker pulverizer. Finally, a mixture of 0.4 g of sample powder and 4 g of $Li_2B_4O_7$ was fused and made into a glass bead for XRF analysis. Accuracy and reproducibility of the major element data are better than ±1% and ±2 % (relative standard deviations), respectively. We also analyzed trace element composition of whole-rock using solution mode ICP-MS (iCAP Qc, ThermoFisher Scientific). Rock powder was digested by acids of HF, HClO4, and HNO3. We also analyzed a reference basalt (JB-2: Jochum et al., 2016), yielding results in good agreement with the certified values (Table S2).

Trace elements of selected melt inclusions and glass in vesiculated groundmass were determined by LA-ICP-MS which is a sector-field type inductively coupled plasma-mass spectrometer (Element XR, ThermoFisher Scientific) combined with femto-second laser ablation (FsLA: OK-Fs2000K, OK Lab.) installed at JAMSTEC (Kimura and Chang, 2012). Ablated spot is 30 μm in diameter and ~20 μm in depth. BCR-2G (basalt standard glass issued by the United States Geological Survey) was used as external calibration standard. Any contaminations from surface and proximal phases were checked by the time-resolving profiles of the signal and turned out to be negligible. During the analysis, 100% normalized major element compositions are also obtained.

The mass-normalized susceptibility of the pumice clasts was measured with a kappabridge (KLY-4; AGICO).

3. Field occurrence of the drift pumice clasts

Pumice clasts that had drifted to the Nansei Islands were first reported from Kita-daito Island by local residents via Twitter (https://twitter.com/ufuagari_jima/status/1445317054043602945) on 5 October 2021. The drift pumice clasts were reported on Kikai Island on 10 October, and they continued to other islands located farther west, subsequently the arrivals were reported from Izu Islands and Boso Peninsula in Mid-November. Pumice clasts traveling to west have arrived at Philippine (23 November) and Taiwan (29 November), while those in the north-eastern side arrived later at Yakushima Island (5 December) and Wakayama Prefecture (13 December) even though these places are not so far away from the Nansei Islands (Fig. 1a). The first identification of the drift pumice clasts on Kita-daito Island was on 5 October, because it was the first day that a ban on coastal access due to high waves caused by a typhoon was lifted. An interview with the local residents suggested that the pumice raft was offshore on 30 September, the day of the typhoon attack (Fig. 1a). On Minami-daito Island, a large amount of drift pumice clasts was also deposited in a coastal area (i.e., Kaigunbo pool). At Kaigunbo pool, some pumice clasts became trapped in crevices up to 1 m above sea level during a normal high tide (Fig. 2a-b). Other occurrences of pumice clasts include those collected on a rocky beach a short distance from the shoreline which was not tide-related (Fig. 2c). These occurrences suggest that the pumice on Minami-daito Island was washed onshore by storm waves (Goto et al., 2011) and were then protected from the rising tide. The samples from Kita- and Minami-daito islands are relatively small in size (up to 5-10 cm).

In contrast, the pumice clasts on Kikai Island and islands farther west were deposited as “moraine-like” features on the shorelines of sandy beaches at high tide (Fig. 2d). At low tide, there were rocks and mudflats on the seaward side of the pumice moraines, but almost no pumice. The amount of pumice deposited varied greatly from the beach to beach, possibly due to the orientation of the beach and the direction of waves and winds on the days around when the pumice was deposited in. The pumice clasts deposited on the sandy beach are occasionally large (>10 cm).

The differences in pumice depositional patterns reflect variations in coastal topography. Given that the coasts of Kita- and Minami-daito islands have steep cliffs and no sandy beaches, almost no pumice was deposited these islands. Kikai Island and islands farther west generally have sandy beaches, and drifting materials are easily beached (and subsequently carried away) depending on the direction of the wind and tide.

The drift pumice clasts described below were collected from Kita- and Minami-daito islands and sandy beaches of Kikai Island, Amami Oshima, and Okinawa Island (Fig. 1a).

4. Pumice classification

The pumice clasts collected from the drifting pumice raft by the RV *Keifu-Maru* (samples 15, 18, and 19 provided by the JMA, herein referred to as FOB-JMA-15, -18, and -19, respectively) have similar characteristics to the drift pumice clasts collected from the Nansei Islands. Notably, the large FOB-JMA-18 sample has a highly vesiculated interior (Fig. 3a-b), whereas such highly vesiculated pumice was rarely observed in the drift pumice clasts collected from the Nansei Islands. Regardless of the deposited locations, the characteristics of drift pumice clasts are similar and they can be classified into six types, based on color and texture: gray, black, brown, pale gray, amber, and streaky (Fig. 3c). The details of each type are described below.

Gray type: This is the most abundant pumice type (>90%). The drift pumice clasts collected by the RV *Keifu-Maru* (samples FOB-JMA-15, 18, and 19) are also classified as this type. The pumice consists mainly of gray-colored vesicular glass, containing dark-colored fragments (Fig. 3a and c) that are termed as black xenoliths (Kato, 1988) or mafic inclusions (Sun et al., 1998), whose appearance is sometimes compared to "chocolate-chip cookie." The fragments are a few millimeters to 1 cm in size. Hereafter, we refer to these as black enclaves. Plagioclase-dominated clot also occurs as dark-colored materials that resemble to "Uzura-ishi (quail's egg stone)" commonly observed as pebbles on the shore of the Ioto Island (e.g., Homma, 1925).

Black type: This type occurs as independent black pumice clasts or together with the gray pumice (Fig. 3c). The independent black pumice clasts are not common, and the sub-clasts in the gray pumice are more common. Most black pumice clasts do not contain elongate vesicles or evidence for ductile deformation.

Brown type: This pumice type occurs occasionally as a transitional form of the gray pumice. The brown-colored part occurs parallel to the elongate groundmass texture.

Pale gray type: The pale gray pumice has a groundmass that is a much darker gray color as compared with the gray type. This type is transitional with the gray pumice.

Amber type: The amber type pumice has an amber-colored vesicular groundmass that contains coarse bubbles (up to several millimeters) and is harder than the other types of pumice.

Streaky type: This type of pumice consists of banded gray and black pumice. The bands of black pumice (up to 5 mm wide) are generally thinner than those of the gray pumice.

In addition to the above six pumice types, some pumice clasts have blocky and glassy surfaces that possibly formed by quenching.

5. Petrography and Geochemistry

5.1 Petrography and mineral chemistry of pumice

The pumice clasts consist mainly of phenocrysts of plagioclase (Pl), clinopyroxene (Cpx), rare olivine (Ol), and a groundmass of vesiculated glass and minor amounts of apatite and opaque minerals (Fig. 4a). Representative mineral and glass analyses are listed in Tables 1–3, and whole-rock compositions determined by XRF spectrometry are listed in Table 4.

Two generations of Ol, Cpx, and Pl were recognized based on optical and electron microscopic observations.

One generation of Ol is phenocrysts or inclusions in Pl phenocrysts in the vesiculated groundmass of the gray and brown pumice, with Mg# values (Mg/[Mg+Fe] × 100) of ~65 and almost free of NiO. A few Ol micro-crystals were observed in the vesiculated glass in groundmass of the black pumice, which are up to ~10 μm in diameter and have a similar composition as the low-Mg Ol (Mg# = ~65).The other type occurs as euhedral phenocrysts in the vesiculated groundmass of black pumice, and has Mg# = 92 (Fig. 4c and g), NiO (up to 0.17 mass%), and Al_2O_3 (~0.019 mass%). This high-Mg Ol has a low-Mg rim with Mg# = ~80 showing a clear diffusion profile of ~20 μm thick (Fig. 4g). High-Mg Ol also occurs in the pale gray pumice, with lower Mg# values of up to 87.

Clinopyroxene occurs as phenocrysts in all pumice types. The Cpx has a diopside (Di) to augite (Aug) composition (Fig. 4e), with Di cores with higher Mg# values (~95) and Aug rims with lower Mg# values (~75). Cpx also occurs as micro-crystals in the vesiculated glass in groundmass of the black and gray pumice, and is Aug with Mg# values of ~75.

Plagioclase occurs as phenocrysts (up to 5 mm in size) in the vesiculated groundmass of gray pumice, and is andesine with Ca-rich cores (An_{45}) and Na-rich rims (An_{33}) (Fig. 4d). Pl in the black pumice is fine-grained (<300 μm) and homogeneous, with $An_{40–45}$. Some Pl that occurs as phenocryst coexisting with Di and micro-crystals in the black enclaves has an anorthite composition with $An_{89–95}$. Rare pargasitic amphibole coexists with the anorthitic plagioclase (Fig. 4f), and dendritic crystals within melt inclusions in high-Mg Ol.

The opaque minerals are generally Ti-bearing magnetite (Mag), while those occurring as inclusions in Pl and Cpx are rarely Fe-sulfide. High-Mg type Ol occasionally contained chromian spinel (Cr-Spl). Plagioclase occasionally contains abundant, brown-colored melt inclusions (Fig. 4a). Melt inclusions in low-Mg Ol are brown-colored, while those in high-Mg Ol are colorless (Fig. 4b).

5.2 Petrography and mineral chemistry of Black enclaves

Black enclaves, typically occurring in the gray pumice, have two types of occurrences, called type-1 and type-2. Type-1 black enclaves have a weakly-vesiculated fine-grained groundmass consisting mainly of Pl, Cpx, Mag, and intergrain glass with phenocrysts of Cpx and Ol (Fig. 5a). Type-2 black enclaves have an equigranular texture and consist of Cpx, Ol, and Pl, with minor amounts of magnetite and intergrain glass (Fig. 5b). Weak vesiculation is also recognized in type-2 black enclaves. Ol phenocrysts in type-1 black enclaves are high-Mg (Mg# = 85) and have NiO contents up to 0.12 mass%. Cpx phenocryst in type-1 black enclaves is diopside composition with Mg# values of 92–95 that decrease to 83 in the augite rims. Pl occurs as fine-grained crystals in the groundmass of type-1 black enclaves, most of which are up to 200 μm in length, and has high anorthite contents of up to An_{87}. In contrast, type-2 black enclaves contain Cpx, Ol, and Pl that have similar compositions as those in the vesicular groundmass of the gray pumice, except for the cores of zoned Pl. Pl in type-2 black enclaves exhibited decrease in anorthite content from core (An_{82}) to rim (An_{32}) (Fig. 5d and e). Intergrain glass of both type-1 and 2 black enclaves exhibit colorless and the black color of the enclaves are derived from the high abundance of magnetite in both types (Fig. 5f-g).

5.3 Glass and whole-rock geochemical compositions

The textures of vesicles vary in the different types of pumice. Gray pumice comprises colorless glass with the elongate vesicles, whereas black pumice has a relatively undeformed vesicle texture and brown-colored glass (Fig. 6a–c). Glass surrounding Pl phenocrysts and melt inclusions in Pl in the gray pumice also exhibited brown-colored (Fig. 4a). Amber pumice has a completely different texture, comprising large bubbles and relatively high glass connectivity (Fig. 6d), resulting in its relatively high hardness.

Vesicular glass in the groundmass is transparent and brown in the black and brown pumices, whereas that in the gray and amber pumice is colorless (Fig. 6a–b). Glass in the pale gray pumice is also colorless, but contains abundant micro-crystals (<~5 μm) visible under an optical microscope, which are either rectangular or circular in shape (Fig. e–f). These black micro-crystals were identified as magnetite by Raman microscopy (Fig. 6g). Brown-colored glass in the pale gray pumice only occurs around or inclusions in phenocrysts. Textural characteristics also vary amongst the different types of pumice. Figure 6c shows a scanning electron microscopy (SEM) image of the contact between black and gray pumice. The gray pumice domain contains highly elongate vesicles as compared with the adjacent black pumice that has a bubble aspect ratio of ~1.

Differences in the brown-colored and colorless glass were further investigated by Raman spectroscopy. The Raman spectrum of the brown-colored glass shows a clear peak at 663 cm^{-1} that is attributed to magnetite (Fig. 6g), even though no micro-crystals were visible under the optical microscope. In contrast, the 663 cm^{-1} peak did not appear in the spectra of the colorless glass in gray and amber pumices.

The glass compositions determined by EMP analyses exhibit trachytic compositions, regardless of the pumice type and glass color (Fig. 7a). In particular, the black and gray pumices have very similar compositions, while the amber pumice is relatively enriched in CaO, MgO, and total FeO (Fig. 7b). Intragrain melt in type-1 black enclaves has lower SiO_2 contents (~62 mass%) as compared with the vesiculated glass, whereas intragrain melt in type-2 black enclaves has similar compositions to vesiculated glass.

Melt inclusions in Pl, augitic Cpx, and low-Mg Ol have similar compositions as the groundmass glass, whereas those in diopsidic Cpx and high-Mg Ol have low SiO_2 contents (SiO_2 = 50–55 mass%) and are basaltic to basaltic-andesitic in composition (Fig. 7a). Basaltic melt inclusions occasionally contain dendritic minerals, which are difficult to analyze. The most SiO_2-rich melt inclusion was discovered in a Aug-Cpx enclosed in Pl, and had a rhyolitic composition with SiO_2 = 68–69 mass% (Fig. 7a).

Whole-rock compositions of the gray, black, and amber pumice clasts were determined by XRF spectrometry, and all had trachytic compositions regardless of pumice type (Fig. 7a). Pale gray and brown pumice grade into gray pumice, and we did not undertake separate whole-rock analyses of these types.

Selected mafic melt inclusions in type-1 black enclaves and vesicular (trachytic) glass of gray pumice are analyzed and shown in spider diagram (Fig. 7c). Groundmass of type-1 black enclave was also measured as the mixture of intergrain melt and groundmass minerals. Figure 7c also shows whole-rock trace element compositions of gray pumice (FOB-JMA-15, 18, 19). The whole-rock composition and the trachytic glass of gray pumice showed similar trace element patterns to that of the 1986 eruption. In contrast, mafic melt inclusions exhibited different patterns such as positive anomaly of Sr, negative anomaly of Pr, Zr, and Hr. Although measured as mixtures, groundmass of type-1 black enclaves exhibited intermediate compositions between trachytic glass and mafic inclusions.

5.4 Magnetic susceptibility of pumice

Mass-normalized magnetic susceptibility was determined on the black and gray pumices (Table 5). The black pumice had a higher magnetic susceptibility than the gray pumice.

6. *P*–*T* calculation

Table 6 summarizes the coexisting mineral and melt assemblages observed in the drift pumice clasts. At least two generations can be clearly identified: (1) those associated with mafic melt, including high-Mg Ol and diopsidic Cpx; and (2) those associated with trachytic melt, including low-Mg Ol, augitic Cpx, Mag, and Pl ($An_{44–33}$).

Temperature conditions of (1) were estimated using the Al-in-Ol thermometer (Coogan, 2014). Given that the high-Mg Ol in the black pumice contains Cr-Spl as inclusion, the compositional pair of an Ol core (Mg# = 92) and Cr-Spl (Cr# [= Cr/(Cr+Al) × 100] = 82) of the black pumice (KGB-1) yielded a temperature of 1226 °C. Another pair of high-Mg Ol (Mg# = 88) and corresponding Cr-Spl inclusion (Cr# = 63) found in the pale gray pumice (AYA-3) yielded a temperature of 1129 °C. This range is well comparable with the suggested uncertainty of the calibration (± 20 °C). Accordingly, the temperature of the injected mafic melt should be around 1200 °C.

Pressure-temperature conditions of (2) were determined using the magnetite geothermometer (Canil and Lacourse, 2020) for Mag inclusions in Cpx (Fig. 4e) and the Cpx single mineral geobarometer (Petrelli et al., 2020) for associated Cpx. Mag in augitic Cpx (FSD-1) yielded ~930°C while pressures for associated Cpx is ~250 MPa. The compositional variation of the analyzed pumice clasts shall affect the P-T estimation but the estimated variation could be smaller than the suggested uncertainties of ± 60 °C and 170 MPa for thermometer and barometer, respectively.

7. Discussion

7.1 Different color types of the drift pumice clasts

Despite the different colors of the pumice clasts, whole-rock compositions of the 2021 FOB pumice are similar. The drift pumice clasts from the 1986 eruption also included gray and black (described as dark-gray in the literature) pumice with similar whole-rock compositions including the Fe_2O_3/FeO ratio (Kato, 1988). Raman spectroscopy revealed that the brown-colored glass contained magnetite, although no micro-crystals were observed under the microscope (Fig. 6g). Such a Raman signature is known to originate from sub-microscopic magnetite nanoparticles (Di Genova et al., 2017; Lerner et al., 2021). Based on transmitted electron microscope (TEM) observations of volcanic glass that revealed a crystal size gap of crystalline nanoparticles between <30 nm and >100 nm, Mujin et al. (2017) defined the term "ultrananolite" for grains smaller than <30 nm and redefined the term "nanolite" (in a strict sense) for a grain size of 30–1000 nm. We did not perform TEM observations and only detected Mag nanoparticles based on Raman spectroscopy. As such, we here use the term nanolite in a broad sense for the grain size, and use to describe the sub-microscopic Mag in our glass samples. The precipitation of Mag nanolites is consistent with the higher magnetic susceptibility of the black pumice as compared with the gray pumice.

Paulick and Franz (1997) documented very similar characteristics for trachytic pumice in the Meidob volcanic field, Sudan. They measured the Fe_2O_3/FeO ratios and magnetic susceptibility for the pumice erupted at 5 ka, which revealed a weak positive correlation between whole-rock Fe_2O_3 contents and magnetic susceptibility. In their study, glass in dark gray pumice was also transparent and brown, and they concluded that the brown color was caused by sub-microscopic Mag precipitation in the glass. Schlinger et al. (1986, 1988) identified nano-crystals of Fe oxides in volcanic glasses by TEM observations. In samples from southern Nevada, the size of the Fe oxide grains was up to 140 nm for a quenched sample, and greater in the sample that was more slowly cooled (up to 800 nm; Schlinger et al., 1988). Schlinger et al. (1986) performed heating experiments on colorless, precipitate-free, glass shards at 950°C for 5 min, which resulted in darkening of the glass and precipitates forming on the scale of TEM analysis.

A recent experimental study by Di Genova et al. (2020) revealed that nanolite precipitation in the basaltic system is a transient phenomenon that is preserved at a high cooling rate of 10–20°C/s, whereas slow cooling allowed microlites to form. In contrast, Cáceres et al. (2021) indicated that slow cooling of <0.5°C/min (0.008 °C/s) is required for nanolite precipitation in rhyolitic system. Di Genova et al. (2020) suggested that a small amount (~ 4 vol.%) of nanoparticles and a shear rate of 3.5 s^{-1} would increase the viscosity by a factor of 10^2 within 100 s of nanolite formation. Given that the brown-colored glass of the present study contains nanolites and that this increased its viscosity, this can explain the less deformed texture of the black pumice as compared with the gray pumice (Fig. 6c).

7.2 Timescales of magma mixing

High-Mg Ol found in type-1 black enclaves and black pumice indicated that the mafic magma injection involved in the 2021 FOB explosive eruption. Black pumice clasts are the evidence of heating by the mafic magma of ~1200°C and the clear diffusion profile at the rim recorded the timescales of the magma mixing.

To assess the timescales of the mafic magma injection, diffusion modeling of Fe–Mg zoning in Ol was undertaken following the methods of Costa and Dungan (2005) and Viccaro et al. (2016). Diffusion coefficients for Fe–Mg in Ol along *c*-axis were calculated following Costa and Chakraborty (2004):

$$D_c^{\mathrm{Fe-Mg}} = 5380 \times \left(\frac{f_{O2}}{10^{-12}}\right)^{1/6} \times 10^{3\left(\frac{86-\mathrm{Fo}}{100}\right)} exp\left(\frac{-226000}{8.314 \times T(\mathrm{K})}\right) \quad (1)$$

where Fo refers Mg# of olivine and the diffusion coefficients for the other axis are assumed to be:

$$D_c^{\mathrm{Fe-Mg}} \sim 6D_a^{\mathrm{Fe-Mg}} \sim 6D_b^{\mathrm{Fe-Mg}} \quad (2)$$

Therefore, the pressure dependence of the diffusion coefficients was ignored. The following form of Fick's second law (in one dimension) with concentration-dependent diffusion coefficients was used for the diffusion modeling:

$$\frac{\partial C}{\partial t} = \frac{\partial}{\partial x}\left(D \frac{\partial C}{\partial x}\right) \quad (3)$$

Given that the high-Mg Ol had a plateau core composition of Mg# = 92 (Fig. 4g), we used this as the initial value. The rim composition of Mg# = 81 (point A in Fig. 4c) was regarded as the boundary condition at the rim for the calculation (i.e., we used a time-invariant constant composition at the rim). Given that the diffusion rim is very narrow, point B yielded a higher Mg# due to a small mis-location of the analytical site. We fitted between point A and the corresponding side. Analytical points were taken by 4 μm steps and more than 90 points (~400 μm) were involved for the fitting, although only

10 points at the rim side showed a diffusion profile.

In the present study, the crystal orientation was not determined, and thus diffusional anisotropy was not strictly evaluated. The diffusion modeling was performed assuming a direction parallel to the *c*-axis and the calculated time could be up to 36 times larger than that determined. Diffusion coefficients were calculated at T = 1226°C (derived from Ol–Cr-Spl thermometry) and f_{O2} values varying from QFM+1 to +3 following the calibration of Myers and Eugster (1983), although 1226 °C is slightly out of the calibration range.

Given that the temperature of 1226 °C obtained from Ol is the maximum estimate where intragrain diffusion has taken place, it should be noted that the following timescales are the minimum estimates. Figure 4g shows the best-fit model and Figure 7d shows the relationship between the calculated time and f_{O2} values. Assuming that diffusion occurred parallel to the *c*-axis, the calculated time varies from 14 to 31 hours for the f_{O2} range from QFM+1 to +3. Depending on the crystal orientation, the estimated time becomes as long as 50 days.

7.3 Variable pumice types and their role during the explosive eruption

As Mujin & Nakamura (2020) indicated based on the variable degrees of nano- and microlite growth in the lava/pumice of a single eruption, minor components of the drift pumice, such as pale-gray type, may have originated from the rewelded materials that have fallen back in the previous eruptions(s). However, the common occurrence of the black pumice coexisting with the gray type with clear boundary strongly indicates that the black pumice played certain roles in the explosive eruption of FOB in 2021. Mitchell et al. (2021) suggested that the pumice clasts form a floating raft and those that suddenly sink to the seafloor have distinct micro-textures (i.e., the floating pumice has a higher vesicle number density and lower pore space connectivity). This could bias the pumice clasts that were sampled. However, the range of drift pumice clasts sampled does partly represent the nature of the 2021 FOB eruption.

The main gray pumice may represent the main magma in the magma reservoir of the FOB. The texture of type-2 black enclaves suggests an origin from a highly crystalized part of the magma reservoir, such as crystal mush.

In contrast, type-1 black enclaves and high-Mg olivine in black and pale gray pumice record mafic magma involvement. As the groundmass of type-1 black enclaves shows intermediate composition between trachytic and mafic melts (Fig. 7c), type-1 black enclaves represent the mixing nature of the ascending mafic magma and trachytic magma reservoir (Fig. 8). Mafic melt inclusions in both diopsidic Cpx and high-Mg Ol indicate that mafic magma triggered the eruption. Explosive eruption of silicic magma can be triggered by the cryptic mafic magma injection (e.g., Tamura et al., 2003; Shukuno et al., 2006; Tamura et al., 2009). Such involvement are sometimes recognized as co-occurrence of bimodal mafic and silicic clastic materials, although drift pumice clasts in this study all yielded trachytic compositions.

In the present case, black pumice could have been heated by injected mafic magma; however, the whole-rock composition does not change and the high-Mg Ol and Di-Cpx phenocrysts (should be called as xenocrysts) only recorded it. Transport process of xenocrysts from the mafic magma to trachytic magma without changing whole-rock compositions remains unclear. When hydrous mafic magma is injected into resident felsic crystal-rich mushes, mafic magma dramatically crystallizes due to the water escape into the felsic magma and corresponding change in liquidus temperature (Pistone et al., 2017). The solidification of hot mafic magma essentially releases the latent heat that can enhance the rejuvenation of the crystal mush. Injected mafic magma would either (1) get highly solidified and could not be ejected by the eruption, or (2) sink suddenly around the FOB and we cannot obtain such samples from the drift pumice raft.

Despite the similar whole-rock geochemical compositions of the gray and black pumice, we rarely observed a gradual transition between them. Adjacent gray and black pumice generally have clear boundaries and distinct textures (Fig. 6c), indicating the black pumice magma was highly viscous prior to mingling and that the eruption occurred soon after mingling. The diffusion modeling of Ol also showed a short timescale of black pumice activity, from hours to days (Fig. 7d). Fe oxide nanolites are considered to form due to cooling and/or diffusive H_2O loss (Danyushevsky et al., 2002; Di Genova et al., 2017, 2018). The experimental study of Cáceres et al. (2021) indicated that the nucleation of Fe–Ti oxide nanolites occurs at cooling rates of <0.5 °C/min in the rhyolitic system, i.e. too quick quenching cannot make nanolites to occur. Although the whole-rock composition is different in our case, given the temperature difference of mafic magma (1226 °C) and trachytic magma (930 °C), cooling duration of >12 hours produces the cooling rate of <0.5°C/min and would be suitable for the nanolites precipitation in a silicic magma system, which is in good agreement with the timescales estimated from the diffusion modeling. The presence of magmatic nanolites can enhance heterogeneous bubble nucleation and lead to an explosive eruption of silicic magma (Cáseres et al., 2020). Accordingly, it is suggested that the black pumice had become black due to heating by injected mafic magma and subsequent cooling. Then, nanolites-bearing black pumice had involved in the Plinian eruption due to its increased viscosity.

Although the detailed mechanisms of the 2021 FOB Plinian eruption remain unclear, the common and co-occurrence of the nanolite-bearing black pumice within gray pumice might record an important process involved in the explosive eruption. To sum up, ascending mafic magma evidenced by the melt inclusions in high-Mg Ol and diopsidic Cpx heated a certain amount of trachytic magma reservoir under FOB, triggering the 2021 explosive eruption (Fig. 8). More detailed micro-textural observations of the mingled black and gray pumice clasts and/or streaky pumice might provide further insights into the magmatic systems of the FOB and neighboring volcanoes in the Mariana arc.

Supplementary Materials

Trace element analysis data of vesiculated glass, mafic melt inclusions, and whole-rock (Table S1) as well as the reference standard material (Table S2) are available from the online depository materials.

Acknowledgements

The authors are grateful to S. Hadana of the Kitadaito Island Development Support Organization and T. Komagoe of the Kikai Institute for Coral Reef Science for their help with the field survey and providing pumice samples. We also thank Y. Maruya of the National Outfitters Training School Okinawa Branch (NPO) for discussions about the field observations at Okinawa Island. The many twitter account holders that posted about the FOB pumice are also thanked. We also thank the Japan Meteorological Agency for providing pumice samples. This research was partly supported by the JSPS KAKENHI (grant nos. JP19K14825 and JP19H01999 to K.Y. and JP21H01195 to Y. T.), the Joint Usage and Research Program of the Earthquake Research Institute, the University of Tokyo (ERI JURP 2021-B-01), and NOZOMI Farm. This paper also benefited from constructive reviews by two anonymous reviewers and editorial handling by T. Tsujimori.

References

Aoki, K., Miyazawa, Y., Hihara, T., & Miyama, T. (2020) An objective method for probabilistic forecasting of multimodal Kuroshio states using ensemble simulation and machine learning. Journal of Physical Oceanography, 50, 3189-3204.

Bryan, S.E., Cook, A.G., Evans, J.P., Hebden, K., Hurrey, L., Colls, P., Jell, J.S., Weatherly, D., and Firn, J. (2012) Rapid, long-distance dispersal by pumice rafting. (2012) Plos one, 7, e40583.

Canil, D. & Lacourse, T. (2020) Geothermometry using minor and trace elements in igneous and hydrothermal magnetite. Chemical Geology, 541, 119576.

Cáseres, F., Wadsworth, F.B., Scheu, B., Colombier, M., Madonna, C., Cimarelli, C., Hess, K.-U., Kaliwoda, M., Ruthensteiner, B., & Dingwell, D.B. (2020) Can nanolites enhance eruption explosivity? Geology, 48, 997-1001.

Cáceres, F., Scheu, B., Hess, K.-U., Cimarelli, C., Vasseur, J., Kaliwoda, M., Dingwell, D.B. (2021) From melt to crystals: The effects of cooling on Fe–Ti oxide nanolites crystallization and melt polymerization at oxidizing conditions. Chemical Geology, 563, 120057.

Coogan, L.A., Saunders, A.D., & Wilson, R.N. Aluminum-in-olivine thermometry of primitive basalts: Evidence of an anormalously hot mantle source for large igneous provinces. Chemical Geology, 368, 1-10.

Costa, F. & Chakraborty, S. (2004) Decadal time gaps between mafic intrusion and silicic eruption obtained from chemical zoning patterns in olivine: Earth and Planetary Science Letters, 227, 517–530.

Costa, F. & Dungan, M. (2005) Short time scales of magmatic assimilation from diffusion modeling of multiple elements in olivine. Geology, 33, 837-840.

Danyushevsky, L.V., McNeill, A.W., and Sobolev, A.V. (2002) Experimental and petrological studies of melt inclusions in phenocrysts from mantle-derived magmas: An overview of techniques, advantages and complications. Chemical Geology, 183, 5-24.

Di Genova, D., Sicola, S., Romano, C., Vona, A., Fanara, S., and Spina, L. (2017) Effect of iron and nanolites on Raman spectra of volcanic glasses: A reassessment of existing strategies to estimate the water content. Chemical Geology, 475, 76-86.

Di Genova, D., Caracciolo, A., and Kolzenburg, S. (2018) Measureing the degree of “nanolilization” of volcanic glasses: Understanding syn-eruptive processes recorded in melt inclusions. Lithos, 318, 209-218.

Di Genova, D., Brooker, R.A., Mader, H.M., Drewitt, J.W.E., Longo, A., Deubener, J., Neuvillem D.R., Fanara, S., Shebanova, O., Anzellini, S., Arzilli, F., Bamber, E.C., Hennet, L., La Spina, G., Miyajima, N. (2020) In situ observation of nanolite growth in volcanic melt: A driving force for exprosive eruptions. Science Advances, 6, eabb0413.

Furukawa, H. (1995) Annual report of world volcanic eruptions in 1992, Fukutoku-oka-no-ba. Bulletin of Volcanology, 57, 81-82.

Geospatial Information Authority of Japan (2021) https://www.gsi.go.jp/uchusokuchi/20210820fukutokuokanoba.html

Goto, K., Miyagi, K., Kawana, T., Takahashi, J., & Imamura, F. (2011) Emplacement and movement of boulders by known storm waves – Field evidence from the Okinawa Islands, Japan. Marine Geology, 283, 66-78.

Homma, F. (1925) Geological Observation of Sulphur Island, on the Pacific. Globe, 4, 290-309.

Ikegami, F. (2021) Pumice raft dispersion of Fukutoku-oka-no-ba 2021 eruption. The abstract volume of the annual meeting of the Volcanological Society of Japan, A2-02.

Ito, K., Kato, S., Takahashi, M., Saito, A. (2011) Volcanic topography of Fukutoku-Oka-no-ba volcano in Izu-Ogasawara arc after 2010 eruption. Report of Hydrographic and Oceanographic Researches, 47, 9-13.

Japan Meteoric Agency (2021) Monthly volcanic activity reports of Fukutoku-oka-no-ba, 2021 August. https://www.data.jma.go.jp/svd/vois/data/tokyo/STOCK/monthly_v-act_doc/tokyo/21m08/331_21m08.pdf (Webpage title was translated by the authors)

Jochum, K.P., Weis, U., Schwager, B., Stoll, B., Wilson, S.A., Haug, G.H., Andreae, M.O., Enzweiler, J. (2016) Reference values following ISO guidelines for frequently requested rock reference materials. Geostandards and Geoanalytical Research, 40, 333-350.

Kato, Y. (1988) Gray pumice drifted from Fukutoku-oka-no-ba to Ryukyu Islands. Bulletin of the Volcanological Society of Japan Series 2, 33, 21-30 (in Japanese).

Kimura, J.-I. & Chang, Q. (2012) Origin of suppressed matrix effect for improved analytical performance in determination of major and trace elements in anhydrous silicate samples using 200 nm femtosecond laser ablation sector-field inductively coupled plasma mass spectrometry. Journal of Analytical Atomic Spectrometry, 27, 1549-1559.

Mitchell, S.J., Fauria, K., Houghton, B.F., & Carey, R.J. (2021) Sink or float; microtextural controls on the fate of pumice deposition during the 2012 submarine Harve eruption. Bulletin of Volcanology, 83, 80.

Mori, S., Yamashita, H., & Goto, M. (1992) Drifted pumices from Ogasawara Arc to the coast of Sagami Bay. Bulletin of the Hiratsuka City Museum, 15, 1-14.

Mujin, M., Nakamura, M., and Miyake, A. (2017) Eruption style and crystal size distibutions: Crystallization of groundmass nanolites in the 2011 Shinmoedake eruption. American Mineralogist, 102, 2367-2380.

Mujin, M. & Nakamura, M. (2020) Late-stage groundmass differentiation as a record of magma stagnation, fragmentation, and rewelding. Bulletin of Volcanology, 82, 48.

Myers, J. & Eugster, H.P. (1983) The system Fe-Si-O: Oxygen buffer calibrations to 1,500 K. Contributions to Mineralogy and Petrology, 82, 75-90.

Nakano, S. & Kawanabe, Y. (1992) Pumices drifted to Iriomote Island in 1991. Bulletin of the Volcanological Society of Japan, 37, 95-98 (in Japanese).

Nishizawa, A., Ono, T., Sakamoto, H., Matsumoto, Y., Otani, Y. (2002) Ocean bottom seismographic observation at Fukutoku-okanoba submarine volcano. Report of Hydrographic Researches, 38, 101-123.

Oikawa, T., Yanagisawa, H., Ikegami, F., Ishizuka, O., Mizuochi, H., Tomiya, A., Morita, M., Nakano, S., Kawaguchi, R., & Nakamura, M. (2021) The August 2021 Fukutoku Okanoba Eruption in Ogasawara Islands, Japan. The abstract volume of the annual meeting of the Volcanological Society of Japan, P1-34.

Onodera, K., Kato, T., Seo, N. (2003) Crustal structure in the vicinities of Fukutoku-okanoba submarine volcano estimated from gravity and magnetic anomalies. Report of Hydrographic and Oceanographic Researches, 39, 23-31.

Paulick, H. & Franz, G. (1997) The color of pumice: case study on a trachytic fall deposit, Meidob volcanic field, Sudan. Bulltine of Volcanology, 59, 171-185.

Petrelli, M., Caricchi, L., & Perugini, D. (2020) Machine learning thermo-barometry: Application to clinopyroxene-bearing magmas. Journal of Geophysical Research: Solid Earth, 125, e2020JB020130.

Pistone, M., Blundy, J., Brooker, R.A., & EIMF (2017) Water transfer during magma mixing events: Insights into crystal mush rejuvenation and melt extraction process. American Mineralogist, 102, 766-776.

Sato, T., Miyazaki, T., Tamura, Y., Gill, J.B., Jutzeler, M., Senda, R., & Kimura, J.-I. The earliest stage of Izu rear-arc volcanism revealed by drilling at Site U1437, International Ocean Discovery Program Expedition 350. Island Arc, 2020, e12340

Schlinger, C.M., Smith, R.M., Veblen, D.R. (1986) Geologic origin of magnetic volcanic glasses in the KBS tuff. Geology, 14, 959-962.

Schlinger, C.M., Rosenbaum, J.G., Veblen, D.R. (1988) Fe-oxide microcrystals in welded tuff from southern Nevada: Origin of remanence carriers by precipitation in volcanic glass. Geology, 16, 556-559.

Shukuno, H., Tamura, Y., Tani, K., Chang, Q., Suzuki, T. & Fiske, R. S. (2006). Origin of silicic magmas and the compositional gap at Sumisu submarine caldera, Izu-Bonin arc, Japan. *Journal of Volcanology and Geothermal Research,* 156, 187-216.

Sun, C.-H. Stern, R., Yoshida, T., & Kimura, J.-I. (1998) Fukutoku-oka-no-ba Volcano: A new perspective on the Alkalic Volcano Province in the Izu-Bonin-Mariana arc. The Island Arc, 7, 432-442.

Sun, W. & McDonough, W.F. (1989) Chemical and isotopic systematics of oceanic basalts: Implications for mantle composition and processes. Geological Society London Special Publications, 42, 313-345.

Tada, N., Nishikawa, H., Ichihara, H., Watanabe Kayama, H., Kuwatani, T. (2021) Drift of an ocean bottom electromagnetometer from the Bonin to Ryukyu Islands: estimation of the path and travel time by numerical tracking experiments. Earth, Planets and Space, 73, 224.

Tamura, Y., Yuhara, M., Ishii, T., Irino, N. & Shukuno, H. (2003). Andesites and dacites from Daisen volcano, Japan: partial-to-total remelting of an andesite magma body. Journal of Petrology, 44, 2243-2260.

Tamura, Y., Gill, J. B., Tollstrup, D., Kawabata, H., Shukuno, H., Chang, Q., Miyazaki, T., Takahashi, T., Hirahara, Y., Kodaira, S., Ishizuka, O., Suzuki, T., Kido, Y., Fiske, R. S. & Tatsumi, Y. (2009). Silicic magmas in the Izu-Bonin oceanic arc and implications for crustal evolution. Journal of Petrology, 50, 685-723.

Tani, K., Kawabata, H., Chang, Q., Sato, K., & Tatsumi, Y. (2006) Quantitative analyses of silicate rock major and trace elements by X-ray fluorescence spectrometer: Evaluation of analytical precision and sample preparation. Frontier Research on Earth Evolution, 2, 1-8.

Tsuya, H. (1937) On the volcanics of the Huzi Volcanic zone, with special reference to the geology and petrology of the Idu and Southern Islands. Bulletin of Earthquake Research Institute, 15, 215-357.

Uchiyama, Y., Odani, S., Yamanishi, T., Kamidaira, Y., & Mitarai, S. (2016) Impact of mesoscale recirculation of the Kuroshio on asymmetric oceanic structure around Okinawa Island. Journal of Japan Society of Civil Engineers, Ser. B2 (Coastal Engineering), 72, I_481-I_486.

Viccaro, M., Giuffrida, M., Nicotra, E., & Cristofolini, R. (2016) Timescales of magma storage and migration recorded by olivine crystals in basalts of the March-April 2010 eruption at Eyjafjallajökull volcano, Iceland. American Mineralogist, 101, 222-230.

Yoshida, T., Fujiwara, S., & Aoki, K. (1987) Geochemistry of Fukutoku-oka-no-ba submarine volcano, Izu-Ogasawara arc. Research Report of Laboratory of Nuclear Science, Tohoku University, 20, 202-215 (in Japanese).

Figure Caption

Figure 1.

(a) Index map of the Fukutoku-Oka-no-Ba (FOB) located near the Ioto Island, south of mainland Japan. Summary of the arrival reports of drift pumice are shown. The track of the pumice raft originated from 1986's eruption is also shown. Arrival date are based on Twitter posts for 2021 eruption summarized in https://togetter.com/li/1762225, while those of 1986 eruption are taken from Yoshida et al. (1987), Kato (1988), and Mori et al. (1992). Specific events arranged in chronological order is also summarized. The course of typhoon 16 passed along Japanese Islands on the end of September and should have affected on pumice drifting is also shown in green (sourced from Japan Meteorological Agency database, https://www.data.jma.go.jp/yoho/typhoon/route_map/bstv2021.html). Gray dashed line indicates the meandering path of the Kuroshio Current expected in mid-November, 2021 (sourced from YouTube APL Channel by Japan Agency for Marine-earth Science, https://www.youtube.com/channel/UCgxUDhjq8UEKOwrqzC0zpAg) (b) Topographic map around FOB after Ito et al. (2011).

Figure 2.

Field occurrence of the unloaded drift pumice. (a) Kaigunbo artificial pool at the Minami-daito Island. Small drift pumice clasts were observed on the rugged rock on the road, up to approximately 1m height. Pumice clasts on the road were almost removed. (b) Closed view of the orange rectangle of (a), showing remained pumice clasts in the rock crevices. (c) Rocky beach near the Kaigunbo pool. Large number of pumice clasts were collected in the topographic low. The pumice-pooled area was isolated from the sea by a wall-like topographic high of the coastal rocks. (d) Drift pumice clasts unloaded on the sandy beach of the Amami-Oshima Island. Pumice clasts comprised a "pumice moraine" at the high tide shoreline, while clasts did not remain at more seaward rocky area.

Figure 3

Photo of the typical drift pumice clasts. (a) The large sample collected by JMA RV *Keifu-Maru* (FOB-JMA-18). Compared with the drift sample from the Nansei Islands, rugged surface was preserved. (b) Inside of FOB-JMA-18. Central part is highly vesicular compared to the outer part. (c) Variety of pumice clasts collected from the Nansei Islands. Details are described in the text.

Figure 4.

Photomicrograph and SEM images of the phenocryst minerals in the studied pumice. (a) Typical microscopic texture of the gray pumice showing Ol and Pl phenocryst. Brown-colored melt occur as inclusion and surroundings of Pl. (b) Colorless mafic melt inclusion in high-Mg Ol occurred in pale gray pumice. Ol was surrounded by trachytic melt. (c) Euhedral high-Mg Ol occurred in black pumice. Outer-most part show decrease in Mg#. Cr-Spl is included. A-B line indicates the line-profile measurement shown in Figure 4g. (d) Pl + Cpx phenocryst clot occurred in gray pumice. Pl exhibited $An_{\sim44}$ core and $An_{\sim35}$ rim. (e) Cpx phenocryst showing a clear zonation from the diopsidic core to augitic rim. Abundant Mag and melt inclusions were observed in the rim. (f) Amphibole associated with anorthite rich Pl ($An_{\sim95}$) occurring together with Cpx phenocryst in the gray pumice. (g) Mg# line-profile of the high-Mg Ol. (h) Representative Cpx compositions in Ca-Mg-Fe ternary diagram.

Figure 5.

Back-scattered electron images of two-types of black enclave observed in the studied pumice. (a) Type-1 black enclave exhibiting Cpx phenocrysts embedded in a dense groundmass composed of Pl, Cpx, opaque minerals, and intergranular melt. (b) Type-2 black enclave exhibiting equigranular texture of Cpx, Pl, and Ol, filled with intergranular melt. (c) Closed photo of (a) showing fine grains of Cpx, Pl, and opaque minerals. (d) Zoned Pl occurred in type-2 black enclave, showing rim-ward decrease in An content. A-B line indicates the position of the line profile shown in (e). (e) A-B line profile of An content. (f-g) Photomicrograph of the intergrain glass of type-1 and -2 black enclaves, both showing colorless glass.

Figure 6

(a) Photomicrograph of the vesicular glass in gray pumice, almost free from microcrystals. (b) Vesicular glass of black pumice exhibits brown color with fine sticky microcrystals of Cpx and rare Ol. (c) Boundary of the black and gray pumice in BSE image. Gray pumice exhibits extensive elongation. (d) Vesicular glass of amber pumice, exhibiting large size bubbles (>500 μm in diameter), and almost colorless. (e) Vesicular glass of pale gray pumice. Abundant nanolites of sticky-shape and small spot are observed (arrowed). (f) BSE image of the glass of pale gray pumice, showing abundant nanolites in the glass. (g) Typical Raman spectra of the black nanoliter in the pale gray pumice and other glasses. The brown-colored glass of black and brown pumice shows the magnetite peak at 663 cm^{-1} although no crystal is visible under optical microscope observation.

Figure 7.

(a) Total alkali vs SiO_2 diagram of the vesiculated glass and whole-rock of the studied pumice clasts. Also whole-rock analyses of previous studies are shown. (b) MgO-CaO binary diagram of the vesiculated glass of the studied sample. Legends are similar to those of (a). (c) Spider diagram showing trace element compositions of the whole-rock gray pumice (FOB-JMA-15, 18, and 19) determined by solution ICP-MS, and vesiculated glass and selected mafic melt inclusions in FOB-JMA-18 determined by LA-ICP-MS. N-MORB data are sourced from Sun and McDonough (1989). (d) Relationship between the time calculated from the diffusion modeling and applied f_{O2} relative to QFM buffer.

Figure 8.

Schematic picture of the FOB 2021 eruption from the preparing stage (A) to the explosive eruption stage (C). Details are in text.

Tables

Table 1. Representative chemical composition of olivine and clinopyroxene.

Footnote

FeO*: total iron as FeO. Fe^{3+}/Fe^{2+} for clinopyroxene were calculated so that total cation =4 (O=6 basis). Mg# = $Mg/(Mg+Fe^{2+}) \times 100$. B.E.: Black enclave

Table 2. Representative chemical composition of plagioclase and opaque minerals.

Footnote

FeO*: total iron as FeO. Fe^{3+}/Fe^{2+} for opaque minerals were calculated so that sum of Fe^{2+}, Mn, and Mg to be 1 (O=4 basis). Calculations of the Pl endmember were as follows: An = Ca/(Ca+Na+K) ×100, Ab = Na/(Ca+Na+K) ×100, Or = K/(Ca+Na+K) ×100. Cr# = Cr/(Cr+Al) × 100. Mg# = $Mg/(Mg+Fe^{2+}) \times 100$. B.E.: Black enclave

Table 3. Representative chemical composition of volcanic glass determined by EMP analyses.

Footnote

FeO*: total iron as FeO. B.E.: Black enclave

Table 4. XRF whole-rock analyses of the selected pumice samples.

Table 5. Mass-normalized susceptibility of gray and black pumice samples.

Table 6. Summary of the coexisting mineral and melt assemblages.

Table S1. Trace element analyses of glass of inclusions and groundmass, in addition to XRF whole-rock analyses.

Table S2. Trace element analysis of secondary standard (JB-2) and the reference values.

Figure 1

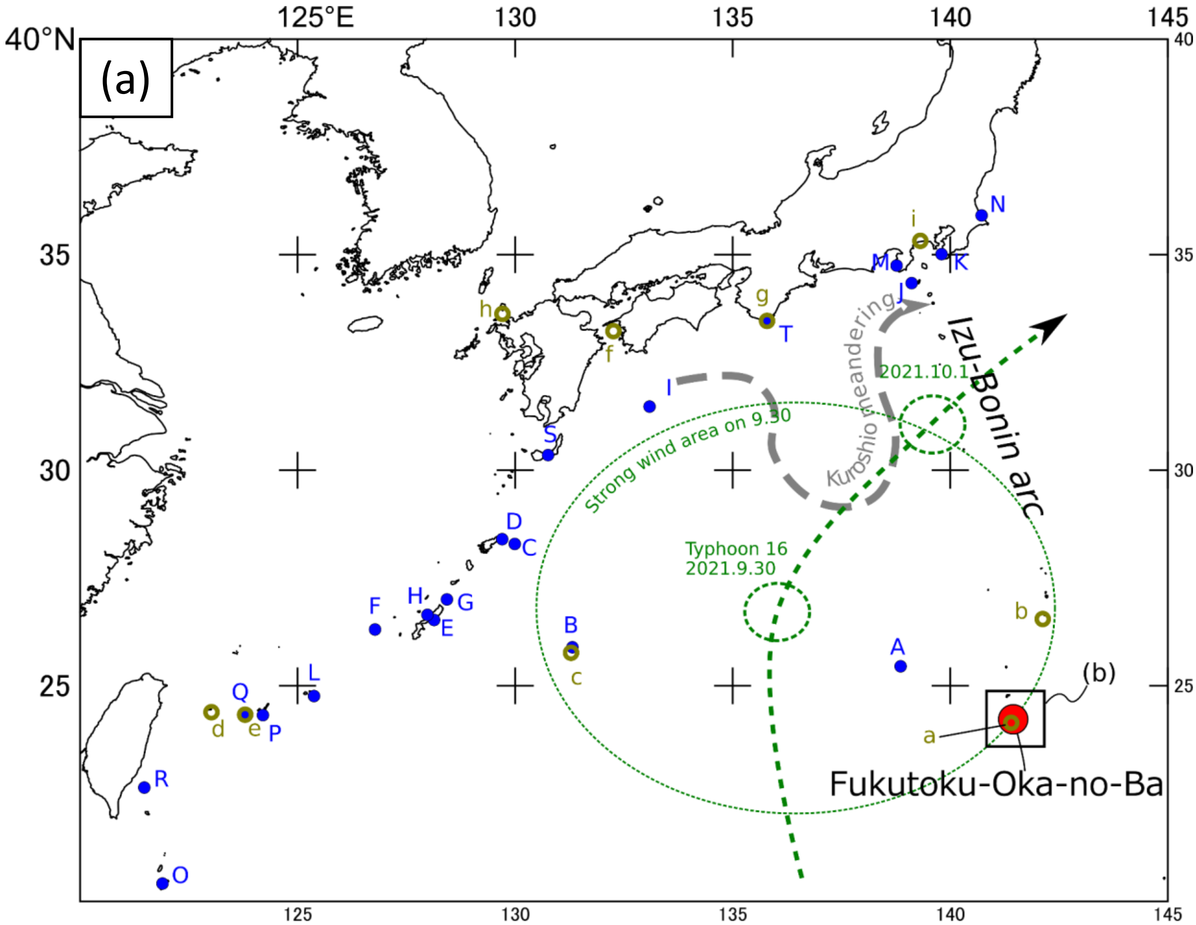

Timeline

2021 Aug. 13 eruption
A: Aug 22 Sampling by RV *Keifu-Maru*
B: Oct. 5 Twitter report from Kita-daito Isl.
C: Oct. 10 Kikai Isl.
D: Oct. 12 Amami-oshima Isl.
E: Oct. 13 Okinawa Main Isl. East coast
F: Oct. 13 Kume Isl.
G: Oct. 14 Yoron Isl.
H: Oct. 18 Okinawa Main Isl. West coast
I:Oct. 30 Aircraft observation of the raft
J: Nov. 10 Shikine Isl.
K: Nov. 15 South Boso Peninsula
L: Nov. 19 Miyako Isl.
M: Nov. 23 South Izu Peninsula
N: Nov. 23 Kashima
O: Nov. 23 Ivana, Batanes Province (PH)
P: Nov. 26 Ishigaki Isl.
Q: Nov. 27 Iriomote Isl.
R: Nov. 29 Taiwan's Green Island
S: Dec. 5 Yakushima/Tanegashima Isl.
T: Dec. 13 Wakayama Pref. Kushimoto

1986 Jan. 18th eruption
a. Jan. 20 Sampling by RV *Takuyo*
b. Mar. 15 Hahajima Isl.
c. Late May Minami-daito Isl.
d. Late May Yonaguni Isl.
e. <June 15 Iriomote Isl.
f. June 26 Ehime Pref. Uwaumi
g. Aug. Wakayama Pref. Kushimoto
h. Oct. Genkai-nada
i. 1991. Sept. Sagami Bay

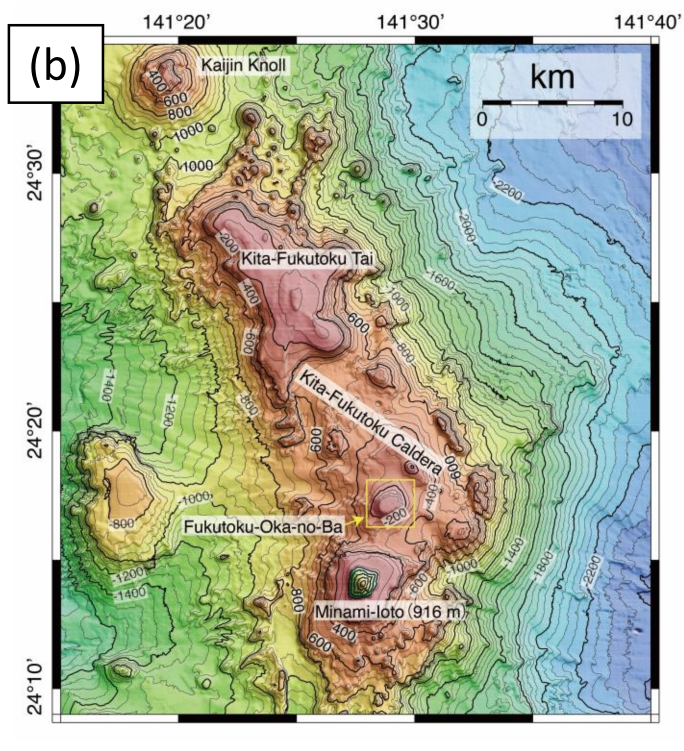

Figure 2

(a)
Maximum height of the
Drifted pumice observed
~1m
sea
(b)
Remained pumice in the rock crevices
5cm
(c)
sea
Topographic high wall
Pumice collected in
the rocky beach
50cm
(d)
No pumice remained on the rocky beach
sea
“Pumice Moraine”

Figure 3

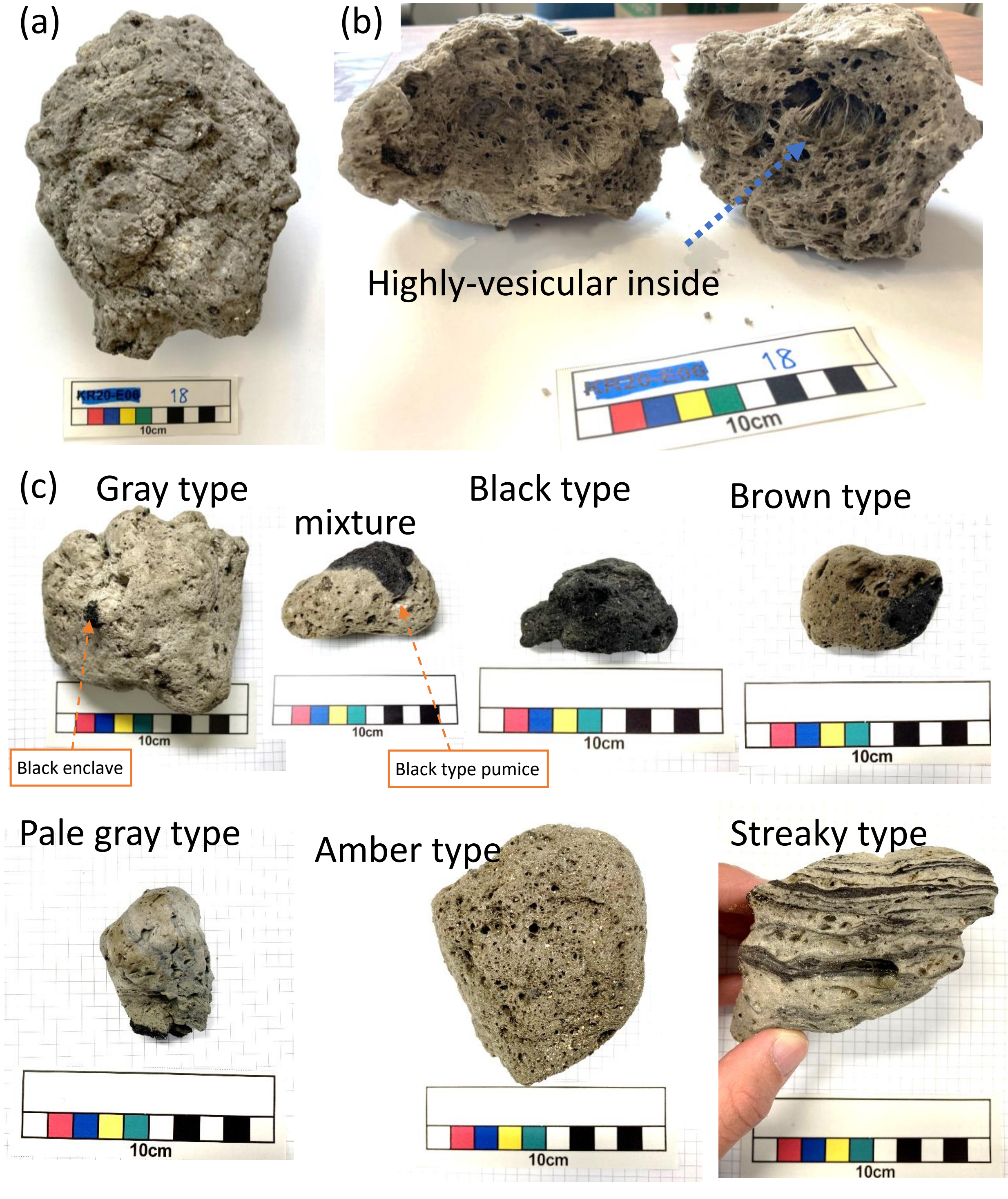
(a)
18
10cm
(b)
Highly-vesicular inside
18
10cm
(c)
Gray type
mixture
Black type
Brown type
Black enclave
Black type pumice
10cm
10cm
10cm
10cm
Pale gray type
Amber type
Streaky type
10cm
10cm
10cm

Figure 4

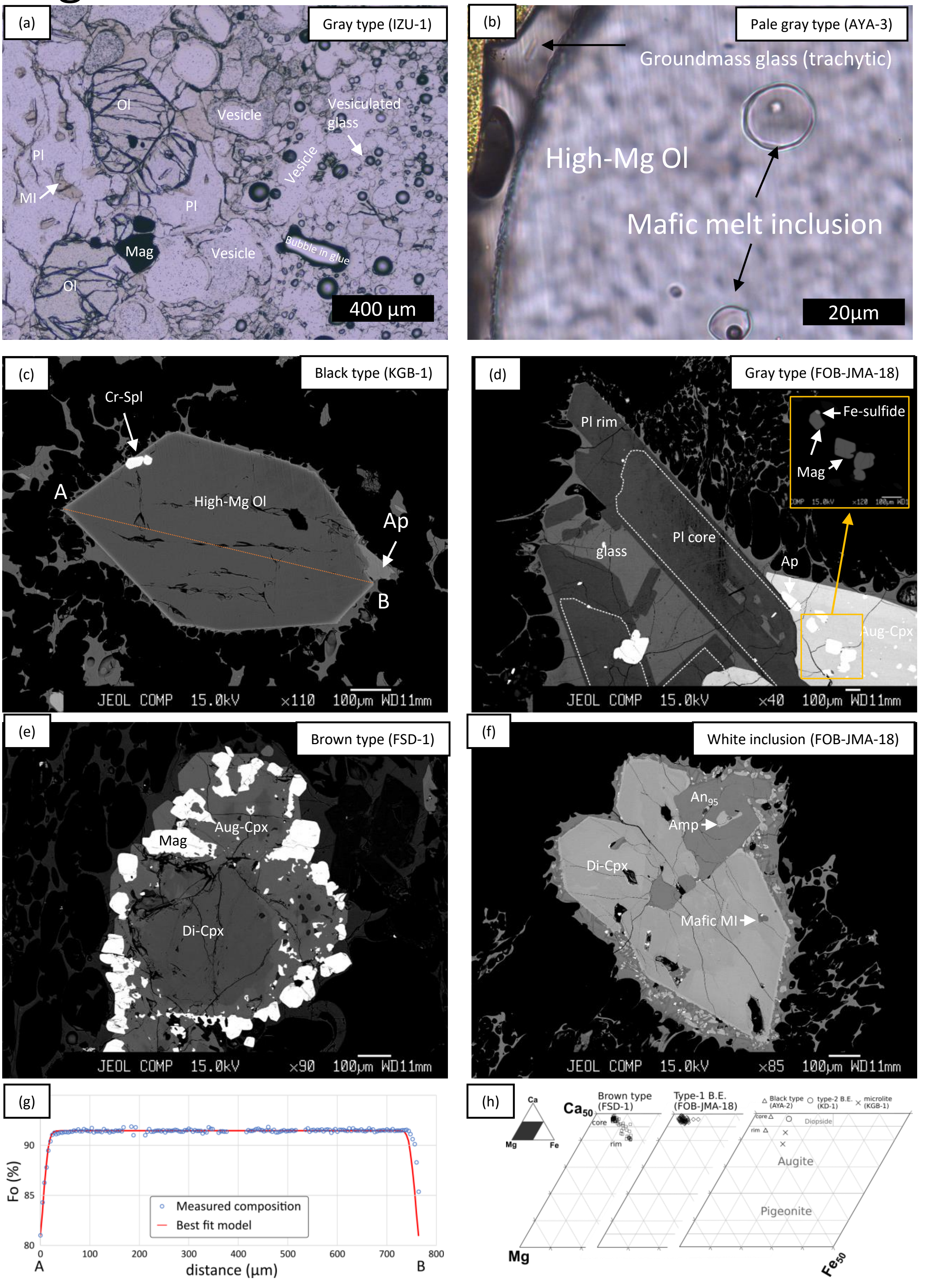

(a)
Gray type (IZU-1)
Ol
Vesicle
Vesiculated glass
Pl
MI
Vesicle
Pl
Mag
Vesicle
Bubble in glue
Ol
400 μm
(b)
Pale gray type (AYA-3)
Groundmass glass (trachytic)
High-Mg Ol
Mafic melt inclusion
20μm
(c)
Black type (KGB-1)
Cr-Spl
A
High-Mg Ol
Ap
B
JEOL COMP 15.0kV ×110 100μm WD11mm
(d)
Gray type (FOB-JMA-18)
Pl rim
Fe-sulfide
Mag
glass
Pl core
Ap
Aug-Cpx
JEOL COMP 15.0kV ×40 100μm WD11mm
(e)
Brown type (FSD-1)
Aug-Cpx
Mag
Di-Cpx
JEOL COMP 15.0kV ×90 100μm WD11mm
(f)
White inclusion (FOB-JMA-18)
An95
Amp
Di-Cpx
Mafic MI
JEOL COMP 15.0kV ×85 100μm WD11mm
(g)
Fo (%)
90
85
80
Measured composition
Best fit model
0 100 200 300 400 500 600 700 800
A
B
distance (μm)
(h)
Ca
Mg
Fe
Ca50
Brown type (FSD-1)
core
rim
Type-1 B.E. (FOB-JMA-18)
Black type (AYA-2)
type-2 B.E. (KD-1)
microlite (KGB-1)
core
rim
Diopside
Augite
Pigeonite
Mg
Fe50

Figure 5

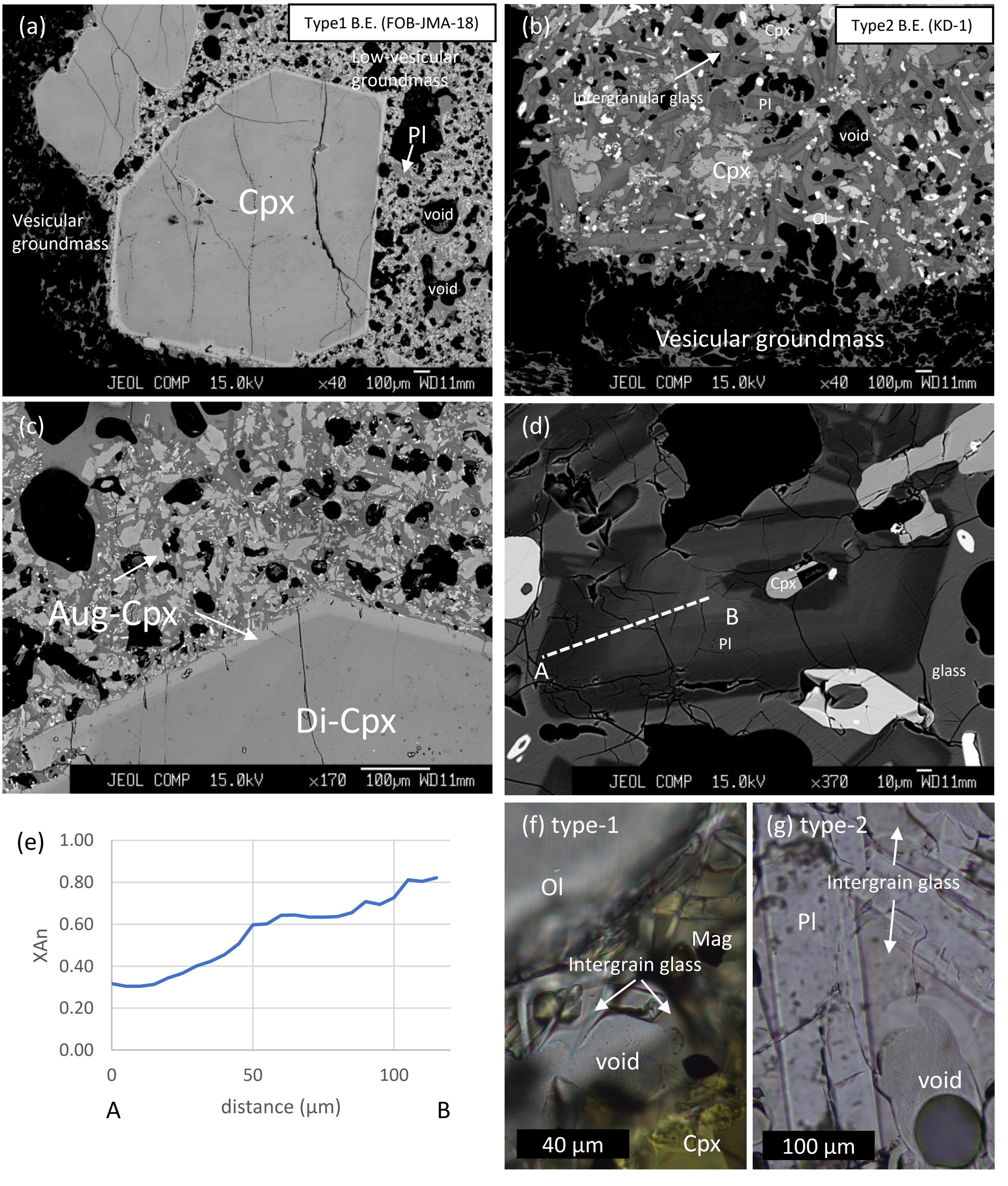

(a)
Type1 B.E. (FOB-JMA-18)
Low-vesicular groundmass
Pl
Cpx
Vesicular groundmass
void
void
JEOL COMP 15.0kV ×40 100μm WD11mm
(b)
Type2 B.E. (KD-1)
Cpx
Intergranular glass
Pl
void
Cpx
Ol
Vesicular groundmass
JEOL COMP 15.0kV ×40 100μm WD11mm
(c)
Aug-Cpx
Di-Cpx
JEOL COMP 15.0kV ×170 100μm WD11mm
(d)
Cpx
B
Pl
A
glass
JEOL COMP 15.0kV ×370 10μm WD11mm
(e)
1.00
0.80
0.60
0.40
0.20
0.00
XAn
0
50
100
A
distance (μm)
B
(f) type-1
Ol
Mag
Intergrain glass
void
40 μm
Cpx
(g) type-2
Intergrain glass
Pl
void
100 μm

Figure 6

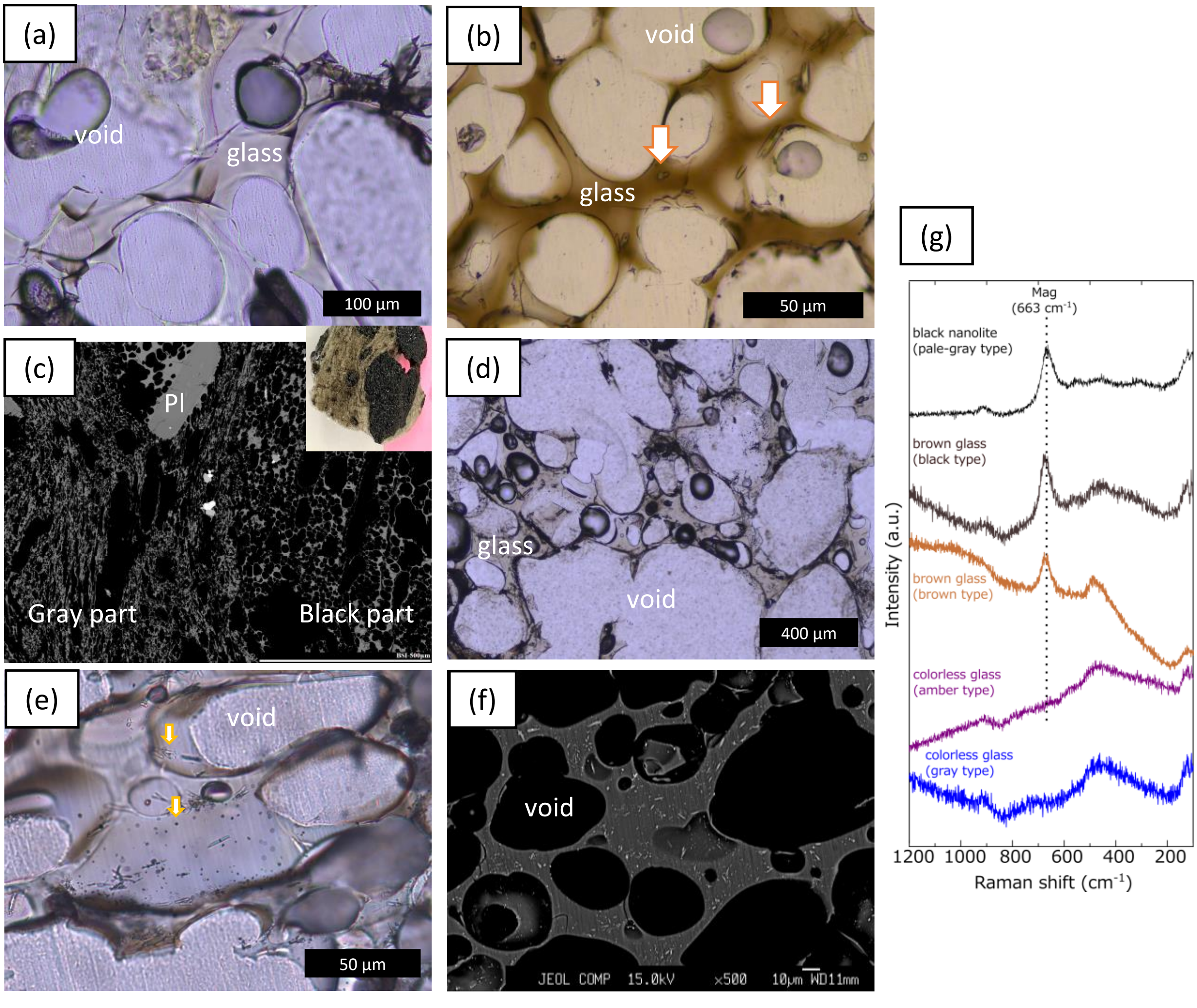
(a)
void
glass
100 µm
(b)
void
glass
50 µm
(c)
Pl
Gray part
Black part
(d)
glass
void
400 µm
(e)
void
50 µm
(f)
void
JEOL COMP 15.0kV ×500 10µm WD11mm
(g)
Mag
(663 cm-1)
black nanolite
(pale-gray type)
brown glass
(black type)
brown glass
(brown type)
colorless glass
(amber type)
colorless glass
(gray type)
Intensity (a.u.)
1200 1000 800 600 400 200
Raman shift (cm-1)

Figure 7

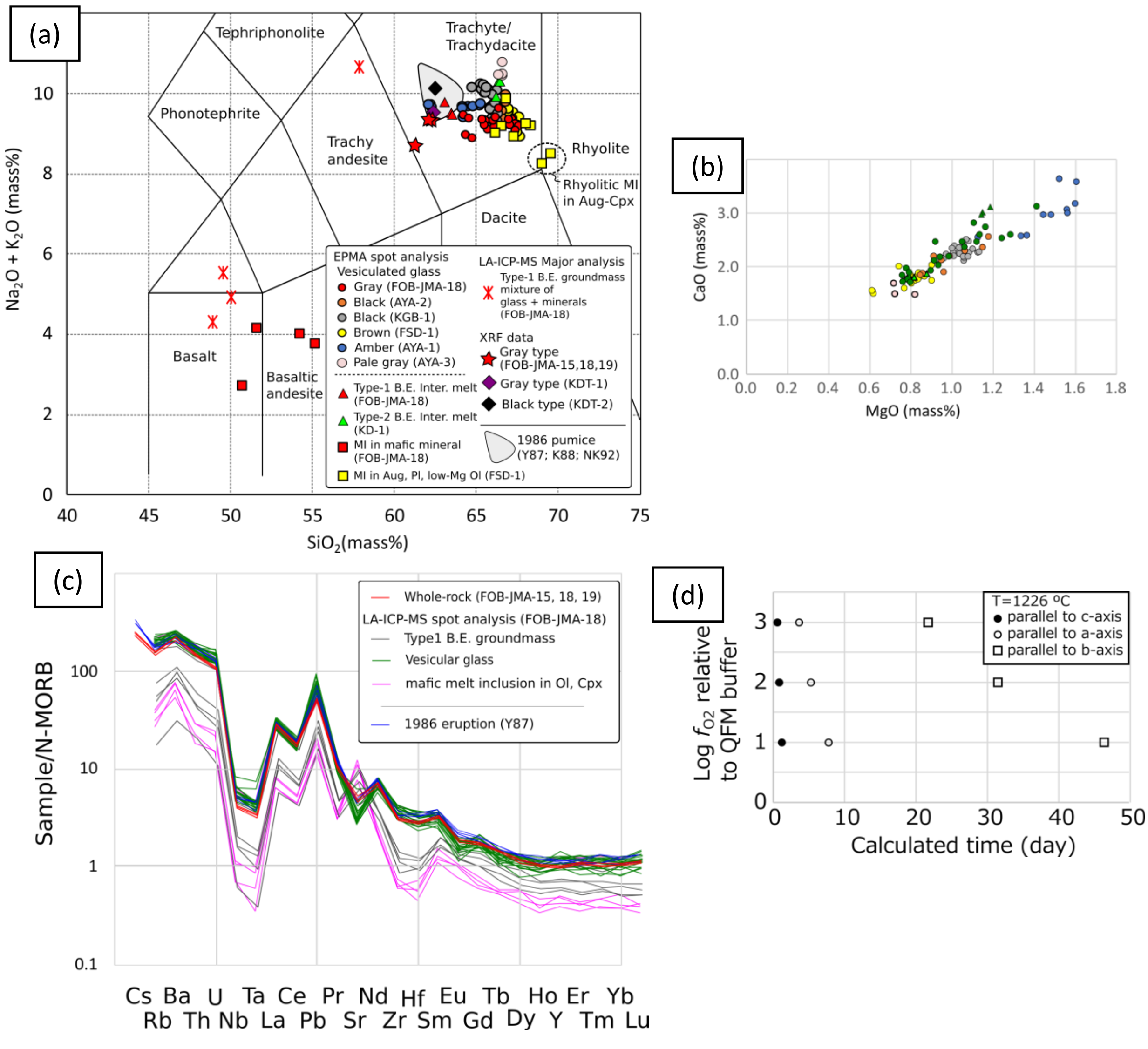

(a)
Tephriphonolite
Trachyte/
Trachydacite
Phonotephrite
Trachy
andesite
Rhyolite
Rhyolitic MI
in Aug-Cpx
Dacite
Basalt
Basaltic
andesite
EPMA spot analysis
Vesiculated glass
Gray (FOB-JMA-18)
Black (AYA-2)
Black (KGB-1)
Brown (FSD-1)
Amber (AYA-1)
Pale gray (AYA-3)
Type-1 B.E. Inter. melt
(FOB-JMA-18)
Type-2 B.E. Inter. melt
(KD-1)
MI in mafic mineral
(FOB-JMA-18)
MI in Aug, Pl, low-Mg Ol (FSD-1)
LA-ICP-MS Major analysis
Type-1 B.E. groundmass
mixture of
glass + minerals
(FOB-JMA-18)
XRF data
Gray type
(FOB-JMA-15,18,19)
Gray type (KDT-1)
Black type (KDT-2)
1986 pumice
(Y87; K88; NK92)
$Na_2O + K_2O$ (mass%)
SiO_2(mass%)
(b)
CaO (mass%)
MgO (mass%)
(c)
Sample/N-MORB
Whole-rock (FOB-JMA-15, 18, 19)
LA-ICP-MS spot analysis (FOB-JMA-18)
Type1 B.E. groundmass
Vesicular glass
mafic melt inclusion in Ol, Cpx
1986 eruption (Y87)
Cs Ba U Ta Ce Pr Nd Hf Eu Tb Ho Er Yb
Rb Th Nb La Pb Sr Zr Sm Gd Dy Y Tm Lu
(d)
Log f_{O2} relative to QFM buffer
Calculated time (day)
T=1226 ºC
parallel to c-axis
parallel to a-axis
parallel to b-axis

Figure 8

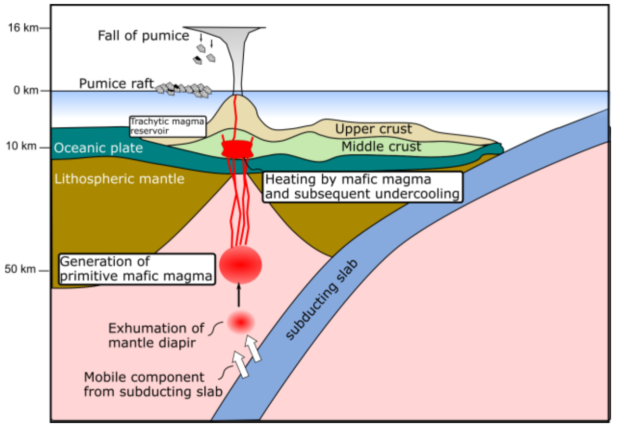
16 km
Fall of pumice
Pumice raft
0 km
Trachytic magma reservoir
Upper crust
Middle crust
10 km
Oceanic plate
Lithospheric mantle
Heating by mafic magma and subsequent undercooling
50 km
Generation of primitive mafic magma
subducting slab
Exhumation of mantle diapir
Mobile component from subducting slab

Table 1

Mineral	Ol					
	Gray	Black			Brown	Amber
site	Pacific ocean	Minami-daito			Amami	Amami
sample No.	FOB-JMA-18	KGB-1			FSD-1	AYA-1
note		core	rim	microlite		
SiO2	35.79	40.22	40.25	34.96	36.37	36.51
TiO2	0.01	0.00	0.01	0.00	0.00	0.00
Al2O3	0.01	0.019	0.040	0.07	0.00	0.00
Cr2O3	0.00	0.01	0.00	0.00	0.01	0.00
FeO*	30.31	8.18	17.47	29.23	29.66	30.29
MnO	1.56	0.15	0.47	1.26	1.52	1.54
MgO	32.39	50.42	41.79	33.79	32.61	32.20
CaO	0.14	0.34	0.18	0.20	0.15	0.15
Na2O	0.00	0.01	0.00	0.00	0.00	0.01
K2O	0.00	0.00	0.01	0.05	0.00	0.01
NiO	0.00	0.17	0.11	0.02	0.00	0.00
Total	100.21	99.53	100.32	99.58	100.32	100.70
O=	4	4	4	4	4	4
Si	0.98	0.99	1.02	0.96	0.99	0.99
Ti	0.00	0.00	0.00	0.00	0.00	0.00
Al	0.00	0.00	0.00	0.00	0.00	0.00
Cr	0.00	0.00	0.00	0.00	0.00	0.00
Fe3+						
Fe2+	0.69	0.17	0.37	0.67	0.67	0.69
Mn	0.04	0.00	0.01	0.03	0.03	0.04
Mg	1.32	1.84	1.58	1.38	1.32	1.30
Ca	0.00	0.01	0.00	0.01	0.00	0.00
Na	0	0.00	0.00	0.00	0.00	0.00
K	0	0.00	0.00	0.00	0.00	0.00
Ni	0.00	0.002	0.002	0.00	0.00	0.00
total cation	3.02	3.01	2.98	3.04	3.01	3.01
Mg#	66	92	81	67	66	65

			Cpx				
Pale Gray	Type-1 B.E.	Type-2 B.E.	Gray		Black		Brown
Amami	Pacific ocean	Kita-daito	Amami		Minami-daito		Amami
AYA-3	FOB-JMA-18	KD-1	AYA-2		KGB-1		FSD-1
			core	rim	core	microlite	core
39.81	38.964	36.737	50.49	49.30	52.12	50.52	51.45
0.00	0	0.035	0.30	0.72	0.27	0.75	0.27
0.02	0.029	0.012	5.10	5.67	3.38	4.26	3.89
0.04	0.016	0	0.00	0.00	0.39	0.02	0.12
11.83	14.226	30.282	6.32	8.92	4.57	8.76	4.28
0.20	0.254	1.498	0.10	0.19	0.00	0.45	0.11
48.02	46.032	32.21	14.62	13.30	15.56	14.52	16.06
0.36	0.336	0.17	23.21	21.34	23.15	19.63	23.76
0.01	0	0.011	0.22	0.33	0.10	0.41	0.07
0.01	0	0.012	0.02	0.01	0.02	0.03	0.02
0.15	0.097	0.005					
100.44	99.95	100.97	100.38	99.79	99.57	99.36	100.03
4	4	4	6	6	6	6	6
0.98	0.98	0.99	1.85	1.83	1.92	1.88	1.88
0.00	0.00	0.00	0.01	0.02	0.01	0.02	0.01
0.00	0.00	0.00	0.22	0.25	0.15	0.19	0.17
0.00	0.00	0.00	0.00	0.00	0.01	0.00	0.00
			0.08	0.06	0.00	0.04	0.07
0.24	0.30	0.68	0.11	0.21	0.14	0.24	0.07
0.00	0.01	0.03	0.00	0.01	0.00	0.01	0.00
1.77	1.72	1.29	0.80	0.74	0.85	0.81	0.87
0.01	0.01	0.00	0.91	0.85	0.91	0.78	0.93
0.00	0.00	0.00	0.02	0.02	0.01	0.03	0.01
0.00	0.00	0.00	0.00	0.00	0.00	0.00	0.00
0.00	0.00	0.00					
3.02	3.02	3.01	4.00	4.00	4.00	4.00	4.00
88	85	65	88	78	86	77	93

		Amber	Pale Gray	Type-1 B.E.		Type-2 B.E.
		Amami	Amami	Pacific ocean		Kita-daito
		AYA-1	AYA-3	FOB-JMA-18		KD-1
rim	host of rhyolitic MI			core	rim	
52.61	53.43	52.48	53.12	53.60	49.23	49.53
0.39	0.32	0.28	0.35	0.20	0.43	0.76
1.48	1.13	3.16	1.15	1.63	4.94	5.49
0.01	0.00	0.17	0.00	0.24	0.07	0.08
9.35	9.91	4.51	9.26	3.21	8.46	9.45
0.83	0.86	0.06	0.78	0.06	0.07	0.42
15.35	15.26	16.05	15.26	17.54	14.63	13.04
19.71	19.50	23.17	19.11	24.24	22.06	21.55
0.45	0.40	0.15	0.39	0.12	0.16	0.39
0.05	0.00	0.01	0.01	0.02	0.01	0.00
100.21	100.82	100.04	99.42	100.87	100.05	100.71
6	6	6	6	6	6	6
1.95	1.97	1.92	1.98	1.93	1.82	1.83
0.01	0.01	0.01	0.01	0.01	0.01	0.02
0.06	0.05	0.14	0.05	0.07	0.22	0.24
0.00	0.00	0.00	0.00	0.01	0.00	0.00
0.06	0.02	0.03	0.00	0.05	0.13	0.09
0.23	0.29	0.11	0.29	0.05	0.13	0.20
0.03	0.03	0.00	0.02	0.00	0.00	0.01
0.85	0.84	0.87	0.85	0.94	0.81	0.72
0.78	0.77	0.91	0.76	0.94	0.87	0.85
0.03	0.03	0.01	0.03	0.01	0.01	0.03
0.00	0.00	0.00	0.00	0.00	0.00	0.00
4.00	4.00	4.00	4.00	4.00	4.00	4.00
79	75	89	75	95	86	78

Table 2

	Pl						
pumice type	Gray		Black	Brown	Amber	Pale Gray	Type-1 B.E.
site	Pacific ocean		Minami-d	Amami	Amami	Amami	Pacific ocean
sample No.	FOB-JMA-18		KGB-1	FSD-1	AYA-1	AYA-3	FOB-JMA-18
note	core	rim					
SiO2	57.33	59.86	57.91	60.18	59.14	59.87	46.27
TiO2	0.05	0.00	0.05	0.00	0.05	0.00	0.05
Al2O3	26.60	24.72	26.54	24.95	25.53	24.83	33.78
Cr2O3	0.12	0.00	0.00	0.01	0.00	0.04	0.00
FeO*	0.56	0.46	0.55	0.58	0.42	0.57	1.05
MnO	0.06	0.00	0.12	0.00	0.00	0.01	0.01
MgO	0.02	0.05	0.04	0.04	0.06	0.09	0.14
CaO	9.00	7.30	9.06	7.09	7.89	7.03	17.35
Na2O	5.81	6.54	5.78	6.57	6.41	6.71	1.39
K2O	0.65	1.06	0.68	1.11	0.89	1.06	0.03
Total	100.18	99.98	100.73	100.52	100.38	100.21	100.07
O=	8	8	8	8	8	8	8
Si	2.57	2.68	2.59	2.68	2.64	2.68	2.13
Ti	0.00	0.00	0.00	0.00	0.00	0.00	0.00
Al	1.41	1.30	1.40	1.31	1.34	1.31	1.84
Cr	0.00	0.00	0.00	0.00	0.00	0.00	0.00
Fe3+	0.00	0.00	0.00	0.00	0.00	0.00	0.00
Fe2+	0.02	0.02	0.02	0.02	0.02	0.02	0.04
Mn	0.00	0.00	0.00	0.00	0.00	0.00	0.00
Mg	0.00	0.00	0.00	0.00	0.00	0.01	0.01
Ca	0.43	0.35	0.43	0.34	0.38	0.34	0.86
Na	0.51	0.57	0.50	0.57	0.55	0.58	0.12
K	0.04	0.06	0.04	0.06	0.05	0.06	0.00
total cation	4.99	4.98	4.98	4.98	4.99	4.99	5.01
An	44	36	45	35	38	34	87
Ab	52	58	51	59	56	59	13
Or	4	6	4	7	5	6	0

		Opaque	Mag	Mag	Cr-Spl	Mag
Type-2 B.E.			Gray	Black	Black	Brown
Kita-daito			Pacific Ocean	Minami-daito	Minami-daito	Amami
KD-1			FOB-JMA-18	KGB-1	KGB-1	FSD-1
core	rim				in high-Mg Ol	in Cpx
48.30	61.17		0.13	0.07	0.09	0.14
0.03	0.03		9.55	10.00	0.25	10.46
32.77	24.29		3.20	2.98	8.34	2.91
0.03	0.03		0.02	0.00	58.20	0.11
0.81	0.56		78.75	78.31	21.82	77.73
0.05	0.00		0.83	0.89	0.31	0.87
0.03	0.03		2.87	2.69	12.54	2.92
16.24	6.17		0.01	0.00	0.02	0.00
1.89	6.50		0.08	0.01	0.00	0.00
0.10	1.29		0.00	0.00	0.00	0.00
100.24	100.06		95.42	94.94	101.57	95.14
8	8		4	4	4	4
2.21	2.72		0.00	0.00	0.00	0.00
0.00	0.00		0.26	0.27	0.01	0.28
1.77	1.28		0.13	0.13	0.32	0.12
0.00	0.00		0.00	0.00	1.48	0.00
0.00	0.00		1.52	1.51	0.19	1.49
0.03	0.02		0.82	0.83	0.39	0.82
0.00	0.00		0.03	0.03	0.01	0.03
0.00	0.00		0.15	0.14	0.60	0.15
0.80	0.29		0.00	0.00	0.00	0.00
0.17	0.56		0.01	0.00	0	0.00
0.01	0.07		0	0	0	0.00
4.99	4.95	Cr#			82	
82	32	Mg#	16	15	60	16
17	60					
1	8					

Mag	Mag	Cr-Spl
Amber	Pale Gray	Pale Gray
Amami	Amami	Amami
AYA-1	AYA-3	AYA-3
		in high-Mg Ol
0.14	0.11	0.11
10.47	9.90	0.50
2.87	2.81	13.69
0.00	0.00	34.33
76.87	77.05	38.83
1.11	1.21	0.32
2.75	2.86	10.49
0.00	0.09	0.02
0.00	0.00	0.07
0.01	0.00	0.01
94.21	94.01	98.37
4	4	4
0.01	0.00	0.00
0.28	0.27	0.01
0.12	0.12	0.52
0.00	0.00	0.88
1.49	1.52	0.57
0.82	0.81	0.49
0.03	0.04	0.01
0.15	0.15	0.51
0.00	0.00	0.00
0.00	0.00	0.00
0.00	0.00	0.00
		63
15	16	51

Table 3

pumice type	Gray	Gray	Black	Amber	Pale gray
site	Pacific ocean	Kita-daito	Minami-daito	Amami	Amami
sample No.	FOB-JMA-18	KD-1	KGB1	AYA1	AYA3
N. analyzed	10	9	22	10	4
note					
SiO2	65.98	66.47	65.36	64.27	65.93
TiO2	0.51	0.52	0.52	0.56	0.52
Al2O3	16.38	16.17	16.31	16.36	16.08
Cr2O3	0.04	0.04	0.02	0.01	0.02
FeO*	3.86	3.54	3.88	4.47	3.57
MnO	0.17	0.16	0.14	0.17	0.14
MgO	0.97	0.80	1.03	1.46	0.76
CaO	2.26	1.84	2.25	3.01	1.60
Na2O	4.62	4.69	4.80	4.82	5.03
K2O	4.93	5.07	4.96	4.83	5.42
P2O5	0.11	0.14	0.14	0.14	0.16
F	0.14	0.14	0.10	0.12	0.11
Cl	0.32	0.31	0.31	0.26	0.32
Total	100.29	99.90	99.81	100.48	99.65

Brown				Type-1 B.E.		
Amami				Pacific ocean		
FSD-1				FOB-JMA-18		
12	2	2	2	2	1	3
	Rhyolitic MI in Cpx	MI in low-Mg Ol	MI in Pl	MI in Cpx	MI in high-Mg Ol	intergranular
66.37	67.67	65.89	66.75	51.92	48.93	62.63
0.56	0.55	0.50	0.37	0.53	0.57	0.33
16.29	16.05	16.15	15.78	20.91	16.39	16.12
0.01	0.03	0.00	0.02	0.08	0.00	0.00
3.91	3.47	3.71	3.34	5.59	9.04	5.83
0.15	0.02	0.14	0.17	0.25	0.18	0.22
0.83	0.34	0.56	0.72	3.43	3.96	1.13
1.78	0.95	1.94	1.57	9.17	14.87	2.97
4.63	4.30	4.67	4.57	2.91	1.78	4.54
4.70	3.98	5.09	4.43	0.91	0.82	4.84
0.14	0.07	0.18	0.07	n.a.	n.a.	0.51
0.12	0.14	0.13	0.16	0.04	0.02	0.21
0.32	0.35	0.39	0.33	0.14	0.09	0.44
99.81	97.90	99.33	97.77	95.68	96.54	99.11

Type-2 B.E.
Kita-daito
KD-1
3
intergranular
65.53
0.41
16.29
0.00
3.95
0.21
0.87
1.85
4.74
5.05
0.20
0.11
0.32
99.11

Table 4

Pumice type	Gray	Gray	Gray	Gray	Black	Amber
site	Pacific ocean	Pacific ocean	Pacific ocean	Kita-daito	Kita-daito	Amami
Sample No.	FOB-JMA-15	FOB-JMA-18	FOB-JMA-19	KD-FOB1	KD-FOB2	AYA-01
SiO_2	60.24	60.50	59.60	60.81	60.85	60.61
TiO_2	0.58	0.58	0.56	0.57	0.61	0.57
Al_2O_3	16.28	15.94	15.35	16.31	16.28	15.52
Fe_2O_3	5.33	5.37	5.55	5.20	5.48	5.66
MnO	0.17	0.17	0.17	0.17	0.18	0.17
MgO	1.93	2.09	3.03	1.82	1.42	3.04
CaO	3.92	3.79	5.03	3.59	3.03	4.49
Na_2O	4.70	4.70	4.33	4.82	5.14	4.55
K_2O	4.34	4.42	4.10	4.43	4.65	4.27
P_2O_5	0.23	0.23	0.21	0.23	0.28	0.22
Total	97.70	97.78	97.93	97.94	97.91	99.10
LOI	1.38	1.47	1.58	0.55	0.78	0.04

Table 5

	weight (g)	bulk mag. Sus. (cm3)	MS (cm3/g)
Gray type	2.996	0.022	7.44E-03
Black type	4.857	0.045	9.23E-03

Table 6

	Mafic member	Trachytic member
Occurrence	Type-1 black enclave xenocryst in black-/ pale gray-type	major member of pumice clasts
melt SiO2	48-55 mass%	62-70 mass%
Ol Mg#	85-92	~65
Cpx composition	diopside	augite
Pl composition	An80-95	An33-44
Other minerals	amphibole (pargasitic), Cr-spinel	magnetite

location	Groundmass materials Type-1 B.E.	Type-1 B.E.	Type-1 B.E.	Type-1 B.E.	MI in Ol Type-1 B.E.	MI in Cpx Type-1 B.E.	MI in Cpx Type-1 B.E.
Major element (100% normalized)							
SiO2	48.93	50.06	49.57	57.86	47.59	49.85	53.52
TiO2	0.81	0.76	0.65	0.57	0.65	0.60	0.55
Al2O3	15.72	17.43	17.56	15.49	15.42	17.91	20.43
FeO	11.29	10.39	12.20	6.31	11.17	8.03	8.32
MnO	0.19	0.18	0.23	0.15	0.19	0.20	0.18
MgO	6.23	4.70	5.50	2.75	6.99	6.28	4.22
CaO	12.40	11.42	8.61	5.99	14.86	13.29	8.26
Na2O	2.87	3.42	3.70	5.47	2.04	2.83	2.91
K2O	1.42	1.49	1.81	5.19	0.93	0.83	1.40
P2O5	0.14	0.17	0.16	0.22	0.14	0.18	0.21
Total	100.00	100.00	100.00	100.00	100.00	100.00	100.00
Trace element (μg/g)							
Sc	39.07	27.75	20.11	18.83	43.91	26.33	9.40
V	468.38	400.42	322.01	118.87	333.18	220.09	271.62
Cr	1.08	0.68	0.47	3.37	6.57	42.25	1.77
Co	40.39	34.71	49.64	18.10	44.34	28.87	30.97
Ni	50.81	35.00	32.44	21.13	149.74	36.25	0.10
Cu	98.11	88.67	188.75	61.55	247.93	271.63	273.86
Zn	87.91	75.32	113.80	84.76	103.05	40.49	75.23
Ga	19.42	19.86	20.27	20.91	20.56	14.54	19.50
Rb	31.80	28.18	42.87	96.04	17.73	15.17	20.81
Sr	676.28	920.07	851.29	391.95	690.31	1120.86	999.71
Y	19.61	16.89	15.98	27.15	13.31	14.15	10.74
Zr	90.65	81.94	103.60	218.74	46.71	44.83	48.92
Nb	3.80	3.67	4.72	10.29	1.60	1.65	2.50
Ba	542.47	623.23	715.81	1137.72	343.09	410.80	464.45
La	25.72	27.65	32.03	62.50	16.13	15.96	20.06
Ce	50.13	51.67	58.38	116.86	32.53	33.56	38.98
Pr	6.17	6.15	6.45	13.25	4.15	4.07	4.41
Nd	25.99	24.71	24.85	47.32	16.10	17.37	16.68
Sm	5.14	4.08	4.39	8.08	3.10	4.06	2.93
Eu	1.33	1.23	1.20	1.63	1.05	1.08	0.79
Gd	4.53	3.60	3.66	6.21	2.67	2.89	2.20
Tb	0.65	0.55	0.47	0.79	0.36	0.39	0.35

Dy	3.38	2.90	2.60	4.42	2.53	2.62	1.87
Ho	0.69	0.59	0.52	0.88	0.47	0.37	0.34
Er	2.06	1.59	1.53	2.91	1.20	1.28	1.05
Tm	0.28	0.27	0.25	0.40	0.21	0.21	0.18
Yb	1.90	1.50	1.56	3.11	1.23	1.61	1.16
Lu	0.26	0.23	0.23	0.54	0.18	0.18	0.15
Hf	2.38	1.85	2.48	5.33	1.47	1.16	0.92
Ta	0.17	0.12	0.19	0.46	0.08	0.05	0.13
Pb	8.16	7.34	9.50	20.05	4.16	4.66	6.37
Th	5.29	5.10	7.12	15.73	2.69	2.23	3.51
U	1.49	1.23	1.91	4.84	0.69	0.73	1.13

B.E.: Black enclave

MI in Cpx	MI in Cpx	Glass				
Type-1 B.E.	Vesiculated glass	Type-1 B.E.	Type-1 B.E.	Type-1 B.E.	Type-1 B.E.	Vesiculated glass
54.67	65.94	63.39	61.12	62.58	63.58	66.05
0.54	0.53	0.57	0.55	0.57	0.50	0.50
20.93	16.03	16.44	15.99	16.49	16.78	15.39
7.06	3.64	4.64	6.30	5.22	4.75	4.65
0.16	0.15	0.15	0.19	0.16	0.16	0.14
3.59	0.83	1.11	2.35	1.14	1.20	1.03
8.38	1.77	2.53	3.39	2.34	2.43	2.38
3.23	5.75	6.01	5.53	6.21	5.65	4.99
1.24	5.16	5.00	4.40	5.08	4.76	4.70
0.20	0.19	0.17	0.19	0.21	0.20	0.17
100.00	100.00	100.00	100.00	100.00	100.00	100.00
6.59	7.17	8.98	11.25	8.53	7.50	7.91
192.45	33.20	74.57	92.02	78.70	63.95	56.04
0.18	-1.20	1.23	0.39	0.26	3.09	1.29
24.68	4.12	8.70	18.15	8.49	8.46	8.72
0.80	-6.26	5.13	6.26	1.15	2.68	-13.09
227.40	9.98	34.37	33.73	68.69	28.76	48.66
54.92	81.59	84.17	93.89	61.22	68.99	88.60
15.51	20.09	21.09	20.12	24.05	21.28	20.35
22.89	122.95	112.61	98.82	133.06	103.45	116.36
1010.20	258.67	320.79	377.11	313.36	338.32	301.50
11.80	35.23	34.81	30.05	35.19	30.44	34.28
55.26	311.51	291.70	250.18	291.52	275.68	293.92
2.63	14.92	13.55	12.12	13.71	12.80	13.56
491.50	1614.16	1652.12	1461.37	1543.15	1438.36	1411.93
21.15	82.55	83.54	70.83	79.03	74.35	73.62
40.68	150.68	157.33	132.84	155.85	130.43	135.23
4.83	16.18	16.64	13.87	16.42	13.74	15.28
19.14	56.23	59.03	53.29	59.64	48.65	54.27
3.35	9.18	9.60	8.51	9.66	7.58	8.81
1.02	1.88	1.86	1.87	1.91	1.78	1.59
2.40	7.36	7.76	6.99	6.06	6.71	6.45
0.38	0.97	0.98	0.92	0.96	0.79	0.88

2.15	5.98	5.85	5.55	5.71	5.40	5.17
0.41	1.11	1.15	1.01	1.14	1.06	1.17
1.24	3.71	3.66	3.25	3.78	3.54	3.22
0.17	0.57	0.54	0.52	0.55	0.49	0.44
1.14	3.78	3.55	3.42	3.35	3.09	3.33
0.19	0.60	0.59	0.52	0.53	0.51	0.55
1.16	7.47	6.68	5.60	6.47	5.74	6.74
0.11	0.61	0.62	0.53	0.53	0.57	0.55
5.75	21.11	24.56	22.29	21.68	20.63	19.34
3.52	22.93	22.11	18.79	21.33	19.82	20.88
1.02	6.42	6.73	5.83	5.40	5.39	6.79

67.06	64.56	64.67	66.81	66.35	67.38	66.17	65.42
0.51	0.55	0.50	0.46	0.47	0.48	0.49	0.55
15.56	15.56	15.20	15.74	14.96	14.48	15.65	15.71
3.57	4.01	4.13	3.31	4.40	3.45	3.87	4.27
0.14	0.16	0.14	0.13	0.14	0.15	0.14	0.17
0.71	1.22	1.79	0.75	1.18	1.02	1.01	1.11
1.60	2.38	2.70	1.84	2.17	1.95	2.05	2.31
5.23	5.77	5.57	5.78	5.42	5.58	5.99	5.35
5.45	5.54	4.97	5.02	4.73	5.36	4.47	4.94
0.16	0.25	0.33	0.16	0.18	0.16	0.17	0.18
100.00	100.00	100.00	100.00	100.00	100.00	100.00	100.00
6.13	7.80	7.89	6.45	7.89	7.26	25.09	8.64
33.30	58.41	51.17	29.63	55.49	47.14	49.45	72.54
0.12	8.03	122.55	0.59	31.65	19.09	261.61	-0.31
3.82	6.47	10.58	3.58	6.74	5.05	9.80	7.50
3.66	-451.99	155.06	-29.73	-17.21	42.06	-3.89	0.54
14.11	14.03	311.83	31.35	30.16	84.67	40.52	31.69
86.59	58.12	85.14	76.92	89.53	80.66	47.20	76.37
20.61	18.59	20.68	19.07	18.06	17.47	24.96	19.21
120.72	121.92	113.16	112.35	120.81	103.64	116.76	109.75
270.78	292.32	301.58	293.05	255.74	250.25	277.42	287.22
34.86	31.51	31.86	30.94	28.95	28.61	41.10	31.41
311.39	274.30	264.40	269.05	241.83	248.85	290.90	271.13
14.93	13.04	12.75	12.95	14.24	12.32	19.95	12.13
1488.64	1397.71	1323.72	1415.72	1266.47	1338.04	1416.69	1477.43
78.41	69.18	66.13	66.13	63.61	67.79	74.86	72.79
145.89	127.05	121.23	124.95	117.96	120.28	134.77	135.13
14.98	13.51	13.43	13.38	12.43	12.69	14.31	14.79
56.71	48.06	47.72	47.51	43.81	48.15	52.82	53.03
9.09	7.82	7.57	8.27	7.14	6.66	9.84	9.31
1.57	1.63	1.46	1.62	1.21	1.33	1.56	1.73
6.30	5.51	5.91	6.22	6.41	6.05	7.25	6.96
0.83	0.90	0.93	0.79	0.77	0.87	0.91	0.75

5.43	5.16	4.52	4.84	3.68	4.64	5.88	5.51
1.05	1.10	0.98	1.00	0.86	0.91	1.13	1.00
3.38	3.37	2.93	3.18	2.59	3.14	3.64	3.25
0.54	0.52	0.46	0.52	0.40	0.38	0.59	0.57
3.90	3.33	2.90	3.15	2.66	3.21	3.72	3.82
0.60	0.54	0.52	0.47	0.44	0.40	0.67	0.55
6.50	6.00	5.49	6.18	5.02	5.97	6.90	7.08
0.61	0.53	0.49	0.50	0.62	0.54	1.01	0.59
21.15	18.53	19.43	16.21	20.78	19.13	27.76	20.74
21.50	20.42	17.79	19.56	17.67	18.12	22.06	21.33
6.95	6.15	5.97	5.81	5.71	5.78	6.49	6.52

						Whole-roc
						Sample
63.34	62.43	65.99	65.15	66.11	62.93	
0.55	0.59	0.55	0.57	0.54	0.51	
16.50	17.32	16.15	15.92	15.85	16.33	
4.59	5.11	3.54	3.87	3.88	3.86	
0.17	0.16	0.15	0.16	0.15	0.15	
1.25	1.27	0.78	0.77	0.77	0.79	
3.47	3.45	1.78	1.75	1.60	1.72	
5.39	5.45	5.66	6.08	5.95	6.32	
4.49	4.03	5.21	5.55	4.99	7.19	
0.25	0.18	0.19	0.17	0.17	0.20	
100.00	100.00	100.00	100.00	100.00	100.00	
8.35	8.08	7.23	6.91	6.38	5.86	Sc
96.84	129.42	35.64	36.76	33.12	43.32	
8.13	-0.03	-0.23	2.66	0.02	10.61	
9.38	11.87	3.67	4.42	4.43	5.07	Co
-3.63	7.30	-14.01	5.01	-6.80	-12.28	Ni
38.93	28.13	12.85	15.00	18.25	12.88	Cu
83.20	88.45	82.30	91.80	76.79	59.02	Cs
21.40	21.20	18.53	22.01	18.98	23.06	Tl
104.00	88.32	113.92	127.90	118.51	125.77	Rb
428.42	583.57	265.46	291.58	273.39	268.74	Sr
30.99	26.93	35.12	37.07	35.29	37.48	Y
243.18	229.55	300.52	331.43	313.55	327.21	Zr
12.28	11.38	14.03	15.64	14.42	16.43	Nb
1606.33	1617.13	1594.06	1695.65	1657.16	1520.71	Ba
79.35	69.30	81.15	85.09	83.29	79.32	La
148.89	131.19	149.99	156.20	151.00	146.19	Ce
15.73	13.77	15.66	17.17	16.68	15.76	Pr
58.65	48.65	54.96	61.65	59.18	53.69	Nd
9.00	8.78	8.54	9.91	9.57	10.44	Sm
1.98	1.68	1.91	2.10	1.88	1.51	Eu
6.81	5.88	6.91	7.42	7.25	8.18	Gd
0.82	0.70	0.91	0.96	1.01	1.05	Tb

5.06	4.86	5.74	6.35	6.06	5.82	Dy
1.08	0.93	1.06	1.31	1.22	1.22	Ho
2.93	2.88	3.70	3.97	3.99	3.60	Er
0.48	0.46	0.55	0.62	0.55	0.62	Tm
3.42	2.53	3.51	3.82	3.50	3.60	Yb
0.57	0.46	0.52	0.70	0.64	0.55	Lu
5.67	5.49	7.20	7.66	7.81	7.48	Hf
0.59	0.53	0.60	0.85	0.62	0.58	Ta
24.48	19.66	20.74	22.71	20.11	28.71	Pb
21.04	18.94	22.09	24.13	22.42	21.36	Th
8.10	5.74	6.34	7.92	7.29	7.37	U

:k trace element analysis

FOB-JMA-15	FOB-JMA-18	FOB-JMA-19
10.025	10.179	16.724
9.552	9.81	12.355
7.963	11.06	19.29
31.291	20.567	31.926
1.713	1.743	1.637
0.226	0.214	0.211
85.932	89.122	82.337
480.516	432.544	414.098
27.861	28.524	26.732
228.595	234.582	218.109
9.581	9.867	9.153
1413.686	1397.824	1291.727
70.377	71.796	66.484
131.345	134.876	125.215
14.059	14.311	13.274
51.504	52.924	49.173
8.566	8.861	8.272
1.913	1.9	1.788
6.302	6.451	6.096
0.965	0.98	0.934

5.173	5.295	4.987
1.042	1.07	0.999
3.204	3.264	3.103
0.47	0.487	0.456
3.227	3.301	3.137
0.511	0.527	0.488
5.743	5.909	5.562
0.441	0.453	0.418
15.293	15.764	14.672
17.514	17.982	16.787
4.992	5.146	4.784

Trace element analysis of secondary standard (JB-2) and the reference value

Sample	JB-2, mea	JB-2, reference* (μg/g)
Sc	54.136	54.08
Co	35.22	37.57
Ni	12.665	14.77
Cu	216.6995	222.1
Rb	5.9045	6.4
Sr	173.1225	178.2
Y	21.242	23.56
Zr	43.7455	48.25
Nb	0.439	0.565
Cs	0.7555	0.8
Ba	208.6435	218.1
La	2.1555	2.281
Ce	6.3355	6.552
Pr	1.0905	1.129
Nd	6.1645	6.392
Sm	2.205	2.266
Eu	0.798	0.836
Gd	3.1625	3.123
Tb	0.5695	0.5863
Dy	3.874	3.868
Ho	0.839	0.863
Er	2.547	2.537
Tm	0.371	0.393
Yb	2.5015	2.529
Lu	0.3825	0.3894
Hf	1.461	1.487
Ta	0.032	0.0396
Tl	0.0355	0.034
Pb	4.965	5.25
Th	0.251	0.2576
U	0.155	0.1528

*Reference of JB-2 is taken from GeoReM database (Jochum et al. Geostand. Geoanal. Res. 40

, 333-350, 2016)